



# A surrogate model for computational homogenization of elastostatics at finite strain using high-dimensional model representation-based neural network

Vien Minh Nguyen-Thanh<sup>1</sup> | Lu Trong Khiem Nguyen<sup>2</sup>  |

Timon Rabczuk<sup>3</sup>  | Xiaoying Zhuang<sup>1,4,5</sup> 

<sup>1</sup>Chair of Computational Science and Simulation Technology, Department of Mathematics and Physics, Leibniz Universität Hannover, Hannover, Germany

<sup>2</sup>Institute of Applied Mechanics, Chair I, University of Stuttgart, Stuttgart, Germany

<sup>3</sup>Institute of Research and Development, Duy Tan University, Da Nang, Vietnam

<sup>4</sup>Heisenberg Professor, PhoenixD Excellence Cluster, Leibniz Universität Hannover, Hannover, Germany

<sup>5</sup>Gottfried Wilhelm Leibniz Universität Hannover

## Correspondence

Timon Rabczuk, Duy Tan University, Institute of Research and Development, 3 Quang Trung, Da Nang, Vietnam.  
Email: timon.rabczuk@uni-weimar.de  
Xiaoying Zhuang, Chair of Computational Science and Simulation Technology, Department of Mathematics and Physics, Leibniz Universität Hannover, Hannover, Germany.  
Email: zhuang@hot.uni-hannover.de

## Funding information

Alexander von Humboldt-Stiftung, Grant/Award Number: Sofja-Kovalevskaja Award

## Summary

We propose a surrogate model for two-scale computational homogenization of elastostatics at finite strains. The macroscopic constitutive law is made numerically available via an explicit formulation of the associated macroenergy density. This energy density is constructed by using a neural network architecture that mimics a high-dimensional model representation. The database for training this network is assembled through solving a set of microscopic boundary value problems with the prescribed macroscopic deformation gradients (input data) and subsequently retrieving the corresponding averaged energies (output data). Therefore, the two-scale computational procedure for nonlinear elasticity can be broken down into two solvers for microscopic and macroscopic equilibrium equations that work separately in two stages, called the offline and online stages. The finite element method is employed to solve the equilibrium equation at the macroscale. As for microscopic problems, an FFT-based collocation method is applied in tandem with the Newton-Raphson iteration and the conjugate-gradient method. Particularly, we solve the microscopic equilibrium equation in the Lippmann-Schwinger form without resorting to the reference medium. In this manner, the fixed-point iteration that might require quite strict numerical stability conditions in the nonlinear regime is avoided. In addition, we derive the projection operator used in the FFT-based method for homogenization of elasticity at finite strain.

## KEYWORDS

computational homogenization, data-driven, FFT-based methods, nonlinear elasticity

## 1 | INTRODUCTION

Multiscale techniques are important for man-made and natural materials; one such approach is homogenization. Roughly speaking, homogenization is a rigorous version of what is known as averaging. It is a powerful tool to study the heterogeneous materials and composites. Based on the knowledge of the microstructure of materials, the objective is to

**Abbreviations:** HDMR, high-dimensional model representation; FFT, fast Fourier transform; FEM, finite element method; NN, neural network.

[Correction added on 23 December 2020, after first online publication: Gottfried Wilhelm Leibniz Universität Hannover was added for Xiaoying Zhuang.]

This is an open access article under the terms of the Creative Commons Attribution-NonCommercial License, which permits use, distribution and reproduction in any medium, provided the original work is properly cited and is not used for commercial purposes.

© 2020 The Authors. *International Journal for Numerical Methods in Engineering* published by John Wiley & Sons Ltd.

understand the response of materials at the macroscale. Homogenization techniques are basically multiscale methods applied to problems where the separation of scales are visible. In the field of homogenization theory for heterogeneous materials, the microscopic length-scale characterizes the fast variation of material properties throughout the continuum while the macroscopic length-scale characterizes dimensions of responses of the entire structure as if the material was homogeneous.

In solid mechanics, analytical homogenization methods have grown fruitfully in the last half century. They include the Hashin-Shtrikman variational principles, which were used to estimate the upper and lower bounds of effective modulus tensor of linear elastic composites for quite general class of microstructures; see, for example, Hashin and Shtrikman,<sup>1,2</sup> Willis,<sup>3,4</sup> Avellaneda,<sup>5</sup> Milton and Kohn,<sup>6</sup> Ponte Castañeda.<sup>7</sup> These works aimed at describing the effective response of the materials of rather random structure whose information is only available through statistical relationship among the composite phases. An extension of the Hashin-Shtrikman (HS) variational principles to nonlinearity was introduced by Willis<sup>8</sup> and subsequently applied to predict the first bounds for nonlinear composites by Talbot and Willis<sup>9</sup> and for viscous composites by Ponte Castañeda et al.<sup>10</sup> The contribution by Ponte Castañeda and Suquet<sup>11</sup> and the monograph by Milton<sup>12</sup> excellently reviewed the variational techniques of homogenization for heterogeneous materials and various topics of composite materials.

Although the fully and semianalytical methods are powerful and able to deliver exact effective response for simple microstructures, they fail to provide good bounds when either the microstructure is complicated or the correlation information between phases is not available. So, computational homogenization methods emerge as promising candidates in the theory of homogenization. One such approach decouples the multiscale problems into two nested problems, namely, the microscopic and macroscopic boundary value problems; see Hughes et al,<sup>13</sup> Miehe et al,<sup>14</sup> Feyel.<sup>15</sup> This approach is called two-scale computational homogenization and normally realized in an FE<sup>2</sup> procedure. Concretely, the original multiscale problem is resolved in a bottom-up fashion in that the macroscopic boundary value problem (BVP) is solved and the effective quantities inquired at the macroscale are supplied after resolving many associated microscopic BVPs; both micro- and macroscopic BVPs are solved by the finite element method (FEM). The microscopic BVP (RVE problem) is solved within a small region of the entire continuum body which is chosen to statistically represent the microstructure of material. Therefore, it is called representative volume element (RVE). The two-scale computational method was made possible, thanks to the crucial theoretical contribution of Mandel<sup>16</sup> and Hill<sup>17</sup> who established a micro-macro transition condition. The latter was coined Hill-Mandel condition or macrohomogeneity condition. It gave rise to appropriate boundary conditions on the RVE problem. A recent review of the state of the art including challenges in the field of computational homogenization was given by Geers et al.<sup>18</sup>

The implementation of the two-scale computational procedure is based on the works by Allaire<sup>19</sup> and Fish et al,<sup>20</sup> who established the appropriate BVPs at the microscale and the macroscale by exploiting asymptotic expansions of the displacements, the strains and the stresses at different length scales. The asymptotic homogenization approach in Fish et al<sup>20</sup> is a generalization of the periodic homogenization theory. They also proposed a numerical implicit integration scheme to deal with plasticity at small strains. With appropriate boundary conditions applied to the RVE, the macrohomogeneity condition can be derived. The two-scale computational procedure can be interpreted as a simple model derived by the asymptotic method because only the solution up to the first-order approximation is considered and all the higher order terms are neglected in the computation (see Fish et al<sup>21</sup>).

As computational cost for meshing in FEM was high for complex microstructure, Moulinec and Suquet<sup>22</sup> published a paper discussing treatment of microscopic BVPs by using the discrete Fourier transform (DFT) spectral method. This paper was a follow-up of an earlier work by the same authors Moulinec and Suquet.<sup>23</sup> An example of a complex microstructure for studying polycrystalline ferroelectric ceramics can be found in Vidyasagar et al.<sup>24</sup> The digital image obtained by scanning electron microscopy can be directly used by resorting to the DFT-based methods as the solution is globally interpolated at the voxels. Therefore, meshing is not necessary. The key idea was to recast a differential equation in terms of the gradient field (such as linearized strain and deformation gradient) into an integral equation resorting to a periodic Green's function. As the DFT can be implemented in a fast algorithm proposed by Cooley and Tukey,<sup>25</sup> it is widely referred to as the fast Fourier transform (FFT). The FFT-based method is a good alternative to the FEM due to several efforts on improving its speed (see Zeman et al<sup>26</sup>) and extensions to microstructures involving high phase contrast and nonlinear materials (see Michel et al<sup>27</sup> and Brisard and Dormieux<sup>28</sup>). Recently, de Geus et al<sup>29</sup> provided a new perspective on the FFT-based collocation method as a Galerkin-based method. Accordingly, the solution method for the equilibrium equation at the microscale combined the Newton-Raphson method and the conjugate-gradient solver. More importantly, the method did not require a set of reference mediums. It has been lately applied to computational homogenization for electroelastically and magnetoelastically coupled materials

in Göküzüm et al.<sup>30</sup> and Rambašek et al.,<sup>31</sup> respectively. These contributions employed a technique of computing the constitutive tangent introduced by Göküzüm and Keip<sup>32</sup> based on the fluctuation sensitivities. A quantitative comparison between some numerical results obtained by the FFT-based method and the FEM can be found in Zeman et al.<sup>33</sup>

A two-scale approach computes the gradient and the hessian of macroenergy density numerically at all quadrature points used in the domain of the macroscopic BVP. In principle, the two-scale method makes the macroenergy density numerically available and supplies the macroscopic solver with derivatives of the energy density by solving the associated microscopic BVPs. On the other hand, it is possible to make the macroenergy density available either in an analytical formulation for simple microstructures or in a numerical approximation such as interpolations, regressions or reduced-order models (ROMs). In the latter case, Yvonnet and He<sup>34</sup> suggested a reduced-order model of multiscale method for studying elastostatics at finite strains. The ROM therein was based on the proper orthogonal decomposition. This work can be classified as data-driven method because it generated the data by solving a sequence of microscopic BVPs and exploited these data to speed up the solution process for the macroscopic BVP. In this manner, the solver for dealing with microscopic BVPs was run concurrently with the macrosolver for the macroscopic BVP. The data of macroscopic strains in their work were assembled in a uniform pattern, but it is generally not a good choice for microstructures exhibiting anisotropy. To overcome this disadvantage, Fritzen and Kunc<sup>35</sup> suggested a specific data sampling strategy. This model was proved to be practically better than the former one by Yvonnet and He<sup>34</sup> because it could handle the composite materials with isotropic and anisotropic microstructures almost equally well. When the two-scale problem consists of the evolution of physical quantities over time in an incremental fashion, the ROMs show tremendous computational benefits (see Oskay and Fish<sup>36</sup>).

Although a two-scale computational homogenization reduces the computational cost of a direct numerical simulation, it can still be significantly improved in some cases. For example, when the composites are made of phases of hyperelastic materials, the effective properties of the homogenized material can be described by a homogenized energy density, or macroscopic free energy density (also called macroenergy density above). In fact, in contrast to Yvonnet and He,<sup>34</sup> Fritzen and Kunc<sup>35</sup> proposed a surrogate model in which the macroscopic free energy density was numerically constructed with the aid of the radial basis functions. A surrogate model replaces the concurrent procedure by separating the series of microscopic BVPs that should be solved in the overall process from the macroscopic BVP. Therefore, it bypasses the repeated process of solving many microscopic BVPs and retrieves the constitutive law. With the surrogate model, the homogenization problem will be solved only at the macroscopic level. In addition, Le et al.<sup>37</sup> proposed to construct the macroenergy density numerically by a neural network architecture that mimics a high-dimensional model representation and reformulated a two-scale computational problem into a surrogate computational model. Note that this work was inspired by a technique of building numerically a potential energy surface, which is an important entity in the community of computational chemistry. As the latter exploited advantages of a high-dimensional model representation, the surrogate model can naturally handle the energy function of high-dimensional variables.

We aim at speeding up the computation for a homogenization problem of elasticity at finite strains by combining the FFT-based collocation method for the microscopic BVPs and a surrogate model based on a neural network architecture proposed by Manzhos and Carrington.<sup>38</sup> Herein, we employed the open-source code provided in accompany with the book by de Borst et al.<sup>39</sup> to solve the macroscopic BVPs. In addition to reduction of computational cost, the explicit macroenergy density can be reused and also improved by enriching the data samples later. Two contributions of the present work are:

- (i) We point out a connection between the approaches presented in Moulinec and Suquet<sup>22</sup> and in de Geus et al.<sup>29</sup> In doing so, we derive compatibility projection operators used in the FFT-based methods.
- (ii) We extend the computational framework in Le et al.<sup>37</sup> to handle the elastostatics at finite strains.

First, the theory of computational homogenization in the context of continuum mechanics is summarized in the following section. The aforementioned highlights (i) and (ii) are presented in Sections 3 and 4, respectively. Also, we discuss some implementation details, which were not addressed in Le et al.<sup>37</sup> Section 5 is devoted to numerical validation of the computational framework via various representative examples. Those include the mathematical problems that admit the analytical solutions as well as the real-world applications. Some concluding remarks are given in the last section.

## 2 | COMPUTATIONAL HOMOGENIZATION FOR FINITE STRAIN PROBLEMS

### 2.1 | Fundamental equations

We summarize the theory of first-order computational homogenization for nonlinear elasticity. The starting point is the variational formulation describing the response of a continuum body of elastic heterogeneous materials. In addition, we briefly go through the fundamentals of continuum mechanics. In this work, we partially adopt the notation and presentation of Miehe et al.<sup>40</sup>

#### 2.1.1 | Deformation of continuum body of heterogeneous materials

Deformation of a continuum body  $B$  can be characterized by the primary field

$$\varphi = \begin{cases} B \times \mathcal{T} & \rightarrow \mathbb{R}^3 \\ (\mathbf{X}, t) & \mapsto \varphi(\mathbf{X}, t) \end{cases}$$

that maps reference coordinates  $\mathbf{X} \in B$  onto points  $\mathbf{x} = \varphi(\mathbf{X}, t)$  of the current configuration  $\varphi(B, t)$ . When the initial time is fixed, this field is called the *deformation mapping* and the *deformation gradient*  $\mathbf{F}$  is defined as its gradient, that is,  $\mathbf{F} = \nabla \varphi$ .

For practical considerations, when the work done by the inertial force is negligible compared with that done by the total stress stored in the system, a static analysis can be used. In this work, we assume that the external force is gradually applied and therefore a classic first-order homogenization theory can be adopted.

We start with the variational formulation: The true motion  $\varphi \in H_{\Gamma_D}^1(B)$  of the continuum body  $B$  is the stationary point of the following potential

$$\Pi(\varphi) = \int_B \psi(\mathbf{X}, \mathbf{F}) \, dV - \int_B \mathbf{f} \cdot \varphi \, dV - \int_{\Gamma_N} \bar{\mathbf{t}} \cdot \varphi \, dA, \quad (1)$$

where  $\Gamma_D$  is a part of the boundary of  $B$  at which the deformation mapping is prescribed,  $\psi(\mathbf{X}, \mathbf{F})$  is the strain energy density,  $\mathbf{f}$  is the external force per unit volume, and  $\bar{\mathbf{t}}$  is the traction force exerted on the body at the boundary  $\Gamma_N$ . In this formulation, the dependence of the energy density on the spatial coordinate  $\mathbf{X}$  indicates heterogeneity of the considered material. The function space

$$H_{\Gamma_D}^1(B) = \{\varphi \in H^1(B) \mid \varphi(\mathbf{X}) = \bar{\varphi}(\mathbf{X}) \quad \forall \mathbf{X} \in \Gamma_D\}$$

is the space of all vector-valued functions in the Sobolev space  $H^1(B)$  that are prescribed on the boundary  $\Gamma_D$  by the given function  $\bar{\varphi}(\mathbf{x})$ . The variational equation derived from the stationary statement  $\delta\Pi = 0$  is the equilibrium equation and the natural boundary conditions

$$\nabla \cdot \mathbf{P}^T = \mathbf{f} \quad \text{in } B, \quad \frac{\partial \psi}{\partial \mathbf{F}} \cdot \mathbf{N} = \bar{\mathbf{t}} \quad \text{on } \Gamma_N,$$

where  $\mathbf{P} = \partial\psi/\partial\mathbf{F}$  is called the first Piola-Kirchhoff stress and  $\mathbf{N} = \mathbf{N}(\mathbf{X})$  is the outward unit vector normal to  $\Gamma_N$  measured in the reference coordinates. The essential boundary condition is

$$\varphi(\mathbf{X}) = \bar{\varphi} \quad \text{on } \Gamma_D.$$

#### 2.1.2 | First-order computational homogenization

Following the theory of first-order computational homogenization, the variational problem defined by (1) can be effectively replaced by a sequence of nested boundary value problems: many microscopic problems and one macroscopic problem.

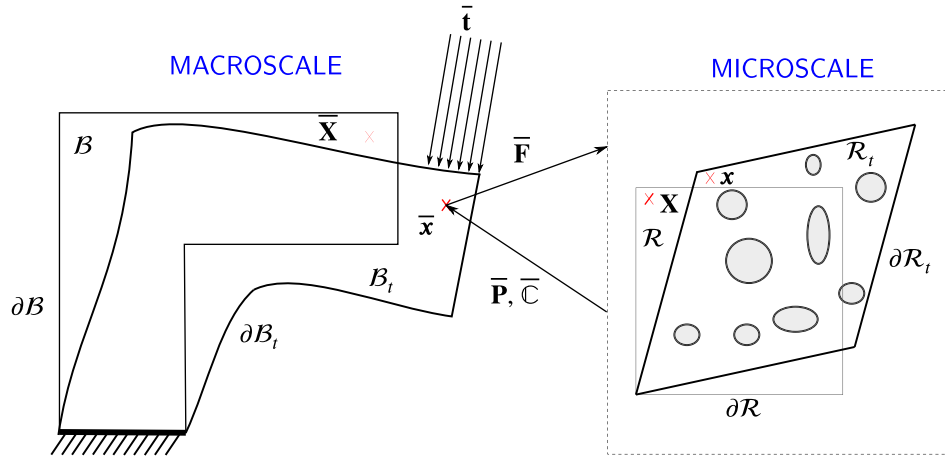


**FIGURE 1** A continuum body of heterogeneous materials. The heterogeneities in the body around the material point  $\bar{\mathbf{X}}$  can be “averaged out” to understand the mechanical response of the body at  $\bar{\mathbf{X}}$  as if it was a homogeneous body by looking at a representative volume element enclosing the material point  $\bar{\mathbf{X}}$ . In this way, we could realize the entire heterogeneous body as the homogeneous one by looking at infinite number of RVEs surrounding all material points [Colour figure can be viewed at [wileyonlinelibrary.com](http://wileyonlinelibrary.com)]

One of the most fundamental assumptions in this theory is the decomposition of the primary field  $\varphi$  about one certain coordinate  $\bar{\mathbf{X}}$  imitating a Taylor expansion as follows:

$$\varphi(\mathbf{X}, t) = \bar{\varphi}_{|\bar{\mathbf{X}}}(t) + \bar{\nabla}(\bar{\varphi}_{|\bar{\mathbf{X}}})(t) \cdot (\mathbf{X} - \bar{\mathbf{X}}) + \tilde{\varphi}(\mathbf{X}, t), \quad \bar{\varphi}_{|\bar{\mathbf{X}}} \in \mathcal{O}(\epsilon^0), \bar{\nabla}(\bar{\varphi}_{|\bar{\mathbf{X}}}) \in \mathcal{O}(\epsilon^0), \tilde{\varphi} \in \mathcal{O}(\epsilon^1),$$

where the subscript  $\bar{\mathbf{X}}$  indicates that the macroscopic field  $\bar{\varphi}$  is associated with such “macroscopic” coordinate and  $\bar{\nabla}$  denotes the differentiation with respect to  $\bar{\mathbf{X}}$  and  $\mathcal{O}$  denotes the standard big-O used in the approximation theory (see Trefethen<sup>41</sup>). In a static analysis, the term  $\bar{\varphi}_{|\bar{\mathbf{X}}}(t)$  can be removed in the subsequent derivation as this term does not contribute to the macroscopic variational problem. We obtain

$$\varphi(\mathbf{X}, t) = \bar{\mathbf{F}}(t) \cdot (\mathbf{X} - \bar{\mathbf{X}}) + \tilde{\varphi}(\mathbf{X}, t), \quad \bar{\mathbf{F}} = \bar{\nabla} \bar{\varphi}. \tag{2}$$

This expansion is valid in a neighborhood of  $\bar{\mathbf{X}}$  called the representative volume element and denoted by  $\mathcal{R}(\bar{\mathbf{X}})$  (see Figure 1). Without ambiguity, we suppress the writing of macroscopic coordinate  $\bar{\mathbf{X}}$  associated with the corresponding RVE. Equation (2) implies that

$$\mathbf{F} := \nabla \varphi = \bar{\mathbf{F}} + \nabla \tilde{\varphi} \quad \Rightarrow \quad \frac{1}{|\mathcal{R}|} \int_{\mathcal{R}} \mathbf{F} \, dV = \bar{\mathbf{F}} + \frac{1}{|\mathcal{R}|} \int_{\mathcal{R}} \nabla \tilde{\varphi} \, dV. \tag{3}$$

In a two-scale computational homogenization, the macroscopic constitutive law is obtained by an appropriate *upscale* of the microscopic quantities resulting from the RVE calculation. This is usually achieved by enforcing the so-called *Hill-Mandel* or *macrohomogeneity* condition. The condition states that the volume average of the variation of work performed on the RVE  $\mathcal{R}(\bar{\mathbf{X}})$  is equal to the local variation of work at  $\bar{\mathbf{X}}$  on the microscale. This condition essentially guarantees energetic consistency in the first-order homogenization theory. It can be derived from the definition of the macroscopic energy density (macroenergy density)

$$\bar{\psi}(\bar{\mathbf{F}}) = \inf_{\varphi \in \mathcal{H}(\bar{\mathbf{F}})} \frac{1}{|\mathcal{R}|} \int_{\mathcal{R}} \psi(\mathbf{X}, \nabla \varphi) \, dV, \tag{4}$$

where  $\mathcal{H}(\bar{\mathbf{F}})$  is the function space of all vector fields that satisfy the decomposition (2) and certain boundary conditions on the RVE boundary  $\partial\mathcal{R}$ . This macroenergy density is not well defined unless a boundary condition for  $\varphi$  is determined, which in turn leaves possibilities for various averaging operators. Let us assume that  $\varphi$  is a stationary point of the above

minimization problem. Then, we can write

$$\bar{\psi}(\bar{\mathbf{F}}) = \frac{1}{|\mathcal{R}|} \int_{\mathcal{R}} \psi \, dV =: \langle \psi \rangle_{\mathcal{R}}$$

and derive the macrohomogeneity condition, or the Hill-Mandel condition, as follows

$$\frac{\partial \bar{\psi}}{\partial \bar{\mathbf{F}}} : \delta \bar{\mathbf{F}} = \left\langle \frac{\partial \psi}{\partial \mathbf{F}} : \delta \mathbf{F} \right\rangle_{\mathcal{R}}. \quad (5)$$

Substitution of Equation (2) into the right-hand side of the above relation leads to

$$\left\langle \frac{\partial \psi}{\partial \mathbf{F}} : \delta \mathbf{F} \right\rangle_{\mathcal{R}} = \frac{1}{|\mathcal{R}|} \int_{\mathcal{R}} \frac{\partial \psi}{\partial \mathbf{F}} : \delta \mathbf{F} \, dV = \frac{1}{|\mathcal{R}|} \int_{\mathcal{R}} \mathbf{P} \, dV : \delta \bar{\mathbf{F}} + \frac{1}{|\mathcal{R}|} \int_{\mathcal{R}} \mathbf{P} : \delta \tilde{\mathbf{F}} \, dV, \quad (6)$$

where we have used the notation

$$\tilde{\mathbf{F}} = \nabla \tilde{\varphi} \quad \Rightarrow \quad \delta \tilde{\mathbf{F}} = \nabla \delta \tilde{\varphi}.$$

Using the Gauss theorem, the last term of Equation (6) can be transformed to the area integral as follows:

$$\frac{1}{|\mathcal{R}|} \int_{\mathcal{R}} \mathbf{P} : \delta \tilde{\mathbf{F}} \, dV = \frac{1}{|\mathcal{R}|} \int_{\partial \mathcal{R}} (\mathbf{P} \cdot \mathbf{N}) \delta \tilde{\varphi} \, dV - \frac{1}{|\mathcal{R}|} \int_{\mathcal{R}} (\nabla \cdot \mathbf{P}^T) \delta \tilde{\varphi} \, dV = \frac{1}{|\mathcal{R}|} \int_{\partial \mathcal{R}} (\mathbf{P} \cdot \mathbf{N}) \delta \tilde{\varphi} \, dV. \quad (7)$$

In this derivation, we have used the assumption that  $\varphi$  is the solution of the minimization problem (4) such that the microscopic equilibrium equation  $\nabla \cdot \mathbf{P}^T = \mathbf{0}$  holds. Combining three Equations (5) to (7), we arrive at

$$\bar{\mathbf{P}} : \delta \bar{\mathbf{F}} = \left( \frac{1}{|\mathcal{R}|} \int_{\mathcal{R}} \mathbf{P} \, dV \right) : \delta \bar{\mathbf{F}} + \frac{1}{|\mathcal{R}|} \int_{\partial \mathcal{R}} (\mathbf{P} \cdot \mathbf{N}) \delta \tilde{\varphi} \, dV,$$

where the macroscopic stress is defined as  $\bar{\mathbf{P}} = \partial \bar{\psi} / \partial \bar{\mathbf{F}}$ . If we choose the boundary condition on  $\varphi$  such that the area integral in the latter condition vanishes, the latter equation will lead to the relation

$$\bar{\mathbf{P}} = \frac{1}{|\mathcal{R}|} \int_{\mathcal{R}} \mathbf{P} \, dV \quad \Leftrightarrow \quad \frac{\partial \bar{\psi}}{\partial \bar{\mathbf{F}}} = \frac{1}{|\mathcal{R}|} \int_{\mathcal{R}} \frac{\partial \psi}{\partial \mathbf{F}} \, dV. \quad (8)$$

The macrohomogeneity condition reduces to the following condition

$$\frac{1}{|\mathcal{R}|} \int_{\mathcal{R}} (\mathbf{P} \cdot \mathbf{N}) \delta \tilde{\varphi} \, dV = \mathbf{0},$$

which can be fulfilled in various ways. Among them, the following three are normally chosen

- Dirichlet boundary condition:  $\tilde{\varphi} = \mathbf{0}$  on  $\partial \mathcal{R}$ .
- Neumann boundary condition:  $\mathbf{P} \cdot \mathbf{N} = \bar{\mathbf{P}} \cdot \mathbf{N}$  on  $\partial \mathcal{R}$ .
- Periodic boundary condition:  $\tilde{\varphi}$  is periodic on  $\partial \mathcal{R}$ . The periodic condition also implies that  $\mathbf{P} \cdot \mathbf{N}$  is antiperiodic on  $\partial \mathcal{R}$ .

It was numerically verified in Terada et al<sup>42</sup> that the periodic condition provided better prediction of the macroscopic response. In addition, we will use the FFT-based collocation method for solving the microscopic problems. Therefore, we adopt in the present work the periodic boundary condition for microscopic problems. The use of weakly periodic boundary conditions is discussed by Fish and Kuznetsov.<sup>43</sup>

To this end, the function space  $\mathcal{H}(\bar{\mathbf{F}})$  is now defined as

$$\mathcal{H}(\bar{\mathbf{F}}) = \{ \varphi = \bar{\mathbf{F}} \cdot (\mathbf{X} - \bar{\mathbf{X}}) + \tilde{\varphi} \in H^1(\mathcal{R}) \mid \tilde{\varphi} \text{ is periodic on } \partial \mathcal{R} \}.$$

The fluctuation fields  $\tilde{\varphi}$  belong to the function space  $\mathcal{H}_\#$  consisting of all vector-valued functions in  $H^1(\mathcal{R})$  that are periodic on  $\partial\mathcal{R}$ . Accordingly, Equation (3) implies that

$$\bar{\mathbf{F}} = \frac{1}{|\mathcal{R}|} \int_{\mathcal{R}} \mathbf{F} \, dV \Leftrightarrow \frac{1}{|\mathcal{R}|} \int_{\mathcal{R}} \tilde{\mathbf{F}} \, dV = \mathbf{0}. \tag{9}$$

Up to the first approximation in the ratio  $\epsilon$  of microscopic and macroscopic length-scales, the macroenergy density will be used as a replacement in the original variational problem (1). In this way, the rapidly varying properties of the heterogeneous materials are “averaged out,” leaving a homogenized elastic body that is characterized by the homogenized free energy density  $\bar{\psi}$  defined in Equation (4). Thus, the presented theory can be transferred to a two-scale computational framework as follows:

- With the macroscopic input  $\bar{\mathbf{F}}$ , we solve the microscopic boundary value problem

$$\bar{\psi}(\bar{\mathbf{F}}) = \inf_{\tilde{\varphi} \in \mathcal{H}_\#} \frac{1}{|\mathcal{R}|} \int_{\mathcal{R}} \psi(\mathbf{X}, \bar{\mathbf{F}} + \nabla \tilde{\varphi}) \, dV \tag{10}$$

for the fluctuation field  $\tilde{\varphi}$  with the periodic boundary condition. Then, we can determine  $\bar{\psi}$  by substituting  $\tilde{\varphi}$  back into Equation (10).

- With the macroenergy density obtained above, we solve the macroscopic boundary value problem: Find the macroscopic deformation mapping  $\bar{\varphi} \in H^1_{\Gamma_D}(B)$  that minimizes the following potential

$$\bar{\Pi}(\bar{\varphi}) = \int_B \bar{\psi}(\bar{\mathbf{F}}) \, dV - \int_B \mathbf{f} \cdot \bar{\varphi} \, dV - \int_{\Gamma_N} \bar{\mathbf{t}} \cdot \bar{\varphi} \, dA. \tag{11}$$

### 3 | METHODOLOGY FOR MICROSCOPIC BOUNDARY VALUE PROBLEM

#### 3.1 | Multidimensional discrete Fourier transform and circular convolution

To present the FFT-based collocation method for multidimensional boundary value problems, we use herein two sets of running indices. The roman letters indicate the indices associated with the collocation nodes used in the discrete Fourier transform, while the greek letters indicate those associated with the problem dimension.

##### 3.1.1 | Discrete Fourier transform and its inverse

Let us consider a periodic function  $V$  defined on domain  $\mathfrak{D}^h = \prod_{\alpha=1}^d (-L_\alpha, L_\alpha)$  of  $d$ -dimension. A uniform mesh of grid points

$$\mathbf{X}_{\mathbf{j}} = ((X_1)_{j_1}, \dots, (X_d)_{j_d}), \quad \mathbf{j} = (j_1, \dots, j_d),$$

with  $(X_\alpha)_{j_\alpha}$  for  $\alpha = 1, \dots, d$  is defined by

$$(X_\alpha)_{j_\alpha} = -L_\alpha + h_\alpha \left( j_\alpha - \frac{1}{2} \right), \quad j_\alpha = 1, \dots, N_\alpha, \quad h_\alpha = \frac{2L_\alpha}{N_\alpha}.$$

We define a periodic *grid function*  $v$  as a restriction of the periodic function on this uniform mesh. The value of  $V$  at node  $\mathbf{X}_{\mathbf{j}}$  is denoted as  $v_{\mathbf{j}} = V(\mathbf{X}_{\mathbf{j}})$ . In this work, we restrict ourselves to the odd numbers of grid points. This means that all  $N_\alpha$  for  $\alpha = 1, \dots, d$  are odd numbers. Hereby, the notation  $\lfloor N_\alpha \rfloor = (N_\alpha - 1)/2$  indicates the floor rounding of  $N_\alpha/2$ .

Multidimensional discrete Fourier transform (DFT) of a multidimensional array  $v_{j_1 \dots j_d}$ , which is a grid function of  $d$  discrete variables  $X_{j_\alpha}$ ,  $\alpha = 1, \dots, d$ , is defined by

$$\hat{v}_{k_1 \dots k_d} = \sum_{j_1=1}^{N_1} \exp[-i \xi_1(k_1)(X_1)_{j_1}] \times \dots \times \sum_{j_d=1}^{N_d} \exp[-i \xi_d(k_d)(X_d)_{j_d}] v_{j_1 \dots j_d}, \quad -[N_\alpha/2] \leq k_\alpha \leq [N_\alpha/2], \quad (12)$$

where  $i = \sqrt{-1}$  is the purely complex unit. In this definition, the *scaled wavenumbers*  $\xi_\alpha = (\pi/L_\alpha) k_\alpha$ ,  $\alpha = 1, \dots, d$ , are defined by scaling the integer wavenumbers  $-[N_\alpha/2] \leq k_\alpha \in \mathbb{Z} \leq [N_\alpha/2]$  by the wavelength ratio  $\pi/L_\alpha$ . Using the notations

$$\mathbf{k} = (k_1, \dots, k_d), \quad \xi(\mathbf{k}) = \left( \frac{\pi}{L_1} k_1, \dots, \frac{\pi}{L_d} k_d \right), \quad \mathbf{j} = (j_1, \dots, j_d), \quad \mathbf{N} = (N_1, \dots, N_d),$$

we will write the full expression of Equation (12) formally as

$$\hat{v}_{\mathbf{k}} = \sum_{\mathbf{j}=1}^{\mathbf{N}} \exp[-i \xi(\mathbf{k}) \cdot \mathbf{X}_{\mathbf{j}}] v_{\mathbf{j}}, \quad -[\mathbf{N}/2] \leq \mathbf{k} \leq [\mathbf{N}/2], \quad (13)$$

in which the summation signifies that all the indices  $j_\alpha$  run from 1 to  $N_\alpha$ . The inverse multidimensional discrete Fourier transform is per definition given by

$$v_{\mathbf{j}} = \frac{1}{|\mathbf{N}|} \sum_{\mathbf{k}=-[\mathbf{N}/2]}^{[\mathbf{N}/2]} \exp[i \xi(\mathbf{k}) \cdot \mathbf{X}_{\mathbf{j}}] \hat{v}_{\mathbf{k}}, \quad \text{where } |\mathbf{N}| = \prod_{\alpha=1}^d N_\alpha. \quad (14)$$

It can be proved that the above definition leads to the true inverse formula of the “forward” discrete Fourier transform (13). It is important to keep in mind that the interpolations accounting for the discrete Fourier transform are derived from the sum of trigonometric functions (see Stein and Shakarchi<sup>44</sup>).

### 3.1.2 | Circular convolution

Let  $V$  and  $W$  be two periodic functions defined on the RVE domain  $\mathcal{R}$ . Then, the convolution of  $V$  and  $W$  is defined as

$$(V * W)(\mathbf{X}) = \int_{\mathcal{R}} V(\mathbf{X} - \mathbf{Y}) W(\mathbf{Y}) d\mathbf{Y} \quad \forall \mathbf{X} \in \mathcal{R},$$

where  $V$  must be extended in a periodic way so that the term  $V(\mathbf{X} - \mathbf{Y})$  is well defined in the above integral. The discrete counterpart of this transformation is then defined by replacing the integral by the summation over all the grid points in  $\mathcal{R}$ . Let  $v$  and  $w$  be the grid functions derived from  $V$  and  $W$ , respectively. It was proven in Stein and Shakarchi<sup>44</sup> that

$$\mathcal{F}[v * w] = \mathcal{F}[v] \mathcal{F}[w] \quad \text{and} \quad v * w = \mathcal{F}^{-1}\{\mathcal{F}[v] \mathcal{F}[w]\}. \quad (15)$$

### 3.2 | Microscopic boundary value problem

It was mentioned in Michel et al<sup>27</sup> that the equilibrium equation in the Lippmann-Schwinger form can be derived by using the Green operator defined in terms of a priori chosen reference medium tensor. On the other hand, the equilibrium of the same form for heterogeneous materials undergoing large deformation was derived in de Geus et al<sup>29</sup> by using the Green operator defined independent from a reference medium. Although the outcome of our formulation is in line with the results obtained in Moulinec and Suquet<sup>22</sup> and de Geus et al,<sup>29</sup> we pursue a different track of presentation. Particularly, we show that their results are connected.



### 3.2.1 | Derivation of microequilibrium with the polarization field

We make a remark regarding the index notation used in the present work. First, all the formulations using index notation adopt the Einstein convention in which the doubly duplicated index implies the summation over it. Second, we use lower case Roman index, such as  $i, j, \dots$  to the mean “with respect to the reference coordinate  $X_i$ .” This practice is different from some literature in that capital letters might be used. Such writing will be beneficial here and there is no ambiguity in doing so. Finally, the index after comma indicates the differentiation with respect to the spatial coordinates. Furthermore, we adopt the terminology “polarization field” from Moulinec and Suquet.<sup>22</sup>

The starting point is the balance equation at the microscale

$$\nabla \cdot \mathbf{P}^T = \mathbf{0} \quad \Leftrightarrow \quad P_{ij,j} = 0.$$

Now, the reference medium  $\mathbb{C}^0$  and the polarization field  $\boldsymbol{\tau}$  are introduced according to

$$P_{ij} = C_{ijkl}^0 F_{kl} - \tau_{ij} \quad \Rightarrow \quad \hat{P}_{ij} = C_{ijkl}^0 \hat{F}_{kl} - \hat{\tau}_{ij}, \tag{16}$$

In the latter equation,  $\mathbb{C}^0$  is only a constant fourth-order tensor that is chosen a priori. Applying the Fourier transform to the balance equation and using the definition  $\mathbf{F} = \nabla \boldsymbol{\varphi}$ , we obtain

$$i \hat{P}_{ij} \xi_j = 0 \quad \Leftrightarrow \quad i (C_{ijkl}^0 i \hat{\varphi}_k \xi_l - \hat{\tau}_{ij}) \xi_j = 0 \quad \Leftrightarrow \quad C_{ijkl}^0 \hat{\varphi}_k \xi_l \xi_j = -i \hat{\tau}_{ij} \xi_j,$$

where we recall that  $i^2 = -1$  and  $\hat{\odot}$  denotes the discrete Fourier transform of  $\odot$  and  $\boldsymbol{\xi}$  is the coordinate in the Fourier space (see Section 3.1). We define the acoustic tensor  $A_{ik}(\boldsymbol{\xi}) = C_{ijkl}^0 \xi_l \xi_j$  and resolve the last equation for  $\hat{\boldsymbol{\varphi}}$  to obtain

$$\hat{\varphi}_k = -i A_{ki}^{-1} \hat{\tau}_{ij} \xi_j \quad \forall \boldsymbol{\xi} \neq \mathbf{0}.$$

Note that the compatibility condition  $\nabla \times \mathbf{F} = \nabla \times \nabla \boldsymbol{\varphi} = \mathbf{0}$  has been fulfilled in such derivation. By using the above equation, we can relate  $\mathbf{F}$  to the polarization tensor  $\boldsymbol{\tau}$  as follows

$$\hat{F}_{ij} = i \hat{\varphi}_i \xi_j = \hat{\Gamma}_{ijkl}^0 \hat{\tau}_{kl}, \quad \text{with } \hat{\Gamma}_{ijkl}^0 = -A_{ik}^{-1} \xi_l \xi_j \quad \forall \boldsymbol{\xi} \neq \mathbf{0}. \tag{17}$$

This relation provides a tool for computing  $\hat{\mathbf{F}}$  at all nonzero wavenumbers in the Fourier space. At zero wavenumbers, we have from the definition of the Fourier transform that

$$\hat{\mathbf{F}}(\boldsymbol{\xi} = \mathbf{0}) = \frac{1}{|\mathcal{R}|} \int_{\mathcal{R}} \mathbf{F} \, dV = \bar{\mathbf{F}}. \tag{18}$$

According to Equations (17), (18), and (15), we define the Green operator  $\boldsymbol{\Gamma}^0$  in the Fourier space as

$$\hat{\Gamma}_{ijkl}^0 = \begin{cases} -A_{ik}^{-1} \xi_l \xi_j & \forall \boldsymbol{\xi} \neq \mathbf{0}, \\ 0 & \boldsymbol{\xi} = \mathbf{0}, \end{cases}$$

and arrive at

$$\mathbf{F} = \bar{\mathbf{F}} + \boldsymbol{\Gamma}^0 * \boldsymbol{\tau}(\mathbf{F}) \quad \Rightarrow \quad \mathbf{F} = \bar{\mathbf{F}} + \boldsymbol{\Gamma}^0 * (\mathbb{C}^0 : \mathbf{F} - \mathbf{P}). \tag{19}$$

If the entire derivation is repeated for the zero-valued stress field  $\mathbf{P}^0 \equiv \mathbf{0}$ , or equivalently from the obviously true equation  $P_{ij,j}^0 = 0$ , we obtain

$$\mathbf{F} = \bar{\mathbf{F}} + \boldsymbol{\Gamma}^0 * (\mathbb{C}^0 : \mathbf{F}). \tag{20}$$

Combining two Equations (19) and (20), we end up with the equilibrium equation at the microscale

$$\mathbf{\Gamma}^0 * \mathbf{P} = \mathbf{0}. \quad (21)$$

### 3.2.2 | Derivation of microequilibrium with compatibility-enforcing operator

We start with the stationary condition of the variational principle (10) as follows: Find  $\mathbf{F} \in V_c(\bar{\mathbf{F}})$  such that

$$\int_{\mathcal{R}} \mathbf{P} : \delta \mathbf{F} \, dV = 0 \quad \forall \delta \mathbf{F} \in V_c(\bar{\mathbf{F}}), \quad (22)$$

where  $V_c(\bar{\mathbf{F}})$  is the space of tensor-valued functions that are compatible in the sense each of them can be derived as gradient of a vector field and that are averaged over the volume of the RVE to give the constant tensor  $\bar{\mathbf{F}}$ . In mathematical terms, the volume-averaging condition is given by (9) and the compatibility condition reads  $\nabla \times \mathbf{F} = \mathbf{0}$ . The function spaces of trial functions and test functions are identical.

Let  $\mathbf{W}$  be a second-order tensor-valued function, then  $\mathbf{\Gamma}^0 * \mathbf{W}$  is a compatible field and its volume average vanishes, that is,

$$\nabla \times (\mathbf{\Gamma}^0 * \mathbf{W}) = \mathbf{0}, \quad \langle \mathbf{\Gamma}^0 * \mathbf{W} \rangle_{\mathcal{R}} = \mathbf{0}. \quad (23)$$

The second condition is a consequence of the specific definition of  $\hat{\mathbf{\Gamma}}^0$  at the zero wavenumbers,  $\hat{\mathbf{\Gamma}}^0(\mathbf{0}) = \mathbf{0}$ . In the index notation, the first equation reads

$$\epsilon_{ijk} (\mathbf{\Gamma}^0_{mkr} * W_{rs})_j = 0 \quad \Rightarrow \quad \epsilon_{ijk} \hat{\Gamma}^0_{mkr} \hat{W}_{rs} i \xi_j = 0 \quad \Rightarrow \quad -\epsilon_{ijk} (A_{mr}^{-1} \xi_s \hat{W}_{rs}) \xi_k \xi_j = 0.$$

We see immediately that  $\epsilon_{ijk} \xi_j \xi_k = 0$  for all  $i$ . Thus, the last equation holds true for all  $i, m = \overline{1, d}$ .

Using the decomposition  $\mathbf{F} = \bar{\mathbf{F}} + \tilde{\mathbf{F}}$  and keeping in mind that  $\mathbf{P} = \mathbf{P}(\bar{\mathbf{F}} + \tilde{\mathbf{F}})$ , Equation (22) can be rewritten as

$$\int_{\mathcal{R}} \mathbf{P} : \delta \tilde{\mathbf{F}} \, dV = \mathbf{0} \quad \forall \delta \tilde{\mathbf{F}} \in V_c(\mathbf{0}).$$

The function space  $V_c(\mathbf{0})$  for the trial and test functions can be relaxed by considering the equivalent variational equation

$$\int_{\mathcal{R}} \mathbf{P} : \delta (\mathbf{\Gamma}^0 * \mathbf{W}) \, dV = 0 \quad \Leftrightarrow \quad \int_{\mathcal{R}} (\mathbf{\Gamma}^0 * \mathbf{P}) : \delta \mathbf{W} \, dV = 0 \quad \forall \delta \mathbf{W}. \quad (24)$$

As Equation (24) must hold true for arbitrary tensor-valued functions  $\delta \mathbf{W}$ , the equilibrium equation (21) can be equivalently derived from this equation. In fact, Equations (21) and (24) are the strong form and weak form of the microscopic boundary value problem (10), respectively.

### 3.2.3 | Compatibility projection operator and connection to the existing works

Even though the equilibrium equation (21) has exactly the same form derived in Geus et al,<sup>29</sup> the main difference is that  $\mathbf{\Gamma}^0$  is not a projection onto the function space  $V_c(\mathbf{0})$ . Indeed, we will point out that the Green function  $\mathbb{G} = \mathbb{C}^0 : \mathbf{\Gamma}^0$  is a projection operator onto the function space  $V_c(\mathbf{0})$ . That means

(i)  $\mathbb{G}$  acting on any arbitrary tensor-valued function  $\mathbf{W}$  produces an element in  $V_c(\mathbf{0})$

$$\nabla \times (\mathbb{G} * \mathbf{W}) = \mathbf{0}, \quad \langle \mathbb{G} * \mathbf{W} \rangle_{\mathcal{R}} = \mathbf{0} \quad \forall \mathbf{W}. \quad (25)$$

(ii)  $\mathbb{G}$  acting on any element  $\mathbf{W}$  in  $V_c(\mathbf{0})$  gives itself

$$\mathbb{G} * [\mathbb{G} * \mathbf{W}] = \mathbb{G} * \mathbf{W} \quad \forall \mathbf{W}. \quad (26)$$

The first property (i) means that  $\mathbb{G}$  projects  $\mathbf{W}$  onto  $V_c(\mathbf{0})$ :  $\mathbb{G}[\mathbf{W}] \in V_c(\mathbf{0})$ , while the second (ii) means  $\mathbb{G}$  is idempotent:  $\mathbb{G}[\mathbb{G}] = \mathbb{G}$ .

First, multiplying Equation (23) by  $\mathbb{C}^0$  on the left-hand side, we obtain

$$\nabla \times [(\mathbb{C}^0 : \Gamma^0) * \mathbf{W}] = \mathbf{0}, \quad \langle (\mathbb{C}^0 : \Gamma^0) * \mathbf{W} \rangle_R = \mathbf{0},$$

which is identical to Equation (25) by identifying  $\mathbb{G} = \mathbb{C}^0 : \Gamma^0$ . Second, let us consider a periodic tensor-valued function  $\mathbf{W}$  with the property  $\langle \mathbf{W} \rangle_R = \mathbf{0}$ , then Equation (20) reduces to

$$\mathbf{W} = \Gamma^0 * (\mathbb{C}^0 : \mathbf{W}) \Rightarrow \mathbf{W} = (\mathbb{C}^0 : \Gamma^0) * \mathbf{W}.$$

This equation implies

$$(\mathbb{C}^0 : \Gamma^0) * \mathbf{W} = (\mathbb{C}^0 : \Gamma^0) * [(\mathbb{C}^0 : \Gamma^0) * \mathbf{W}],$$

which is nothing else but Equation (26).

According to this analysis, various projections can be constructed by choosing different reference elasticity tensor  $\mathbb{C}^0$ . The Green projection operator derived in Geus et al<sup>29</sup> is obtained by setting the reference medium  $\mathbb{C}^0$  to the fourth-order identity tensor:  $\mathbb{C}^0 : \mathbf{W} = \mathbb{I} : \mathbf{W} = \mathbf{W}$ . In that case, we have  $\mathbb{G}^0 = \mathbb{I} : \Gamma^0 = \Gamma^0$  and at the same time

$$C_{ijkl}^0 = \delta_{ik}\delta_{jl} \Rightarrow A_{ik} = \delta_{ik}\delta_{jl}\xi_j\xi_l = \|\xi\|^2\delta_{ik} \Rightarrow \hat{\Gamma}_{ijkl}^0 = -A_{ik}^{-1}\xi_j\xi_l = -\frac{\delta_{ik}}{\|\xi\|^2}\xi_j\xi_l. \tag{27}$$

Thus, among many possibilities of choosing the Green projection operator, we may choose

$$G_{ijkl} = \begin{cases} \frac{\delta_{ik}}{\|\xi\|^2}\xi_j\xi_l & \forall \xi \neq \mathbf{0}, \\ 0 & \xi = \mathbf{0}. \end{cases} \tag{28}$$

As the right-hand side of equilibrium equation (21) is zero, the minus sign appearing in  $\hat{\Gamma}^0$  defined by Equation (28) does not affect the final result. Thus, the minus sign from Equation (27) is drop down to obtain the operator (28). Then, the equilibrium equation at the microscale is equivalent to

$$\mathbb{G} * \mathbf{P} = \mathbf{0}. \tag{29}$$

*Remark*

The above analysis not only leads to the existing results obtained in Michel et al<sup>27</sup> and Geus et al<sup>29</sup> but also draws a connection between the two routes of derivation. At the same time, it reveals that there are many possibilities of choosing projection operators other than (28), each of which is obtained by fixing the reference tensor  $\mathbb{C}^0$ . This outcome extends the result presented in Geus et al.<sup>29</sup>

### 3.3 | Numerical method for microscopic equilibrium equation and macroscopic tangent moduli

We will solve the equilibrium equation defined by (28) and (29) using the Newton-Raphson method (Geus et al<sup>29</sup>). Note that a detailed numerical procedure for the system accounting for magnetoelastostatics can be found in Rambašek et al.<sup>31</sup>

In this contribution, we compare the solutions obtained by a two-scale approach and the proposed surrogate model by means of the resultant macroscopic stress  $\bar{\mathbf{P}}$  and tangent moduli  $\bar{\mathbb{C}}$ . For such comparison, we need to compute these quantities from the solution  $\mathbf{F}$  of the microscopic BVP.

### 3.3.1 | Numerical procedure for microscopic equilibrium

We examine Equation (29) with  $\bar{\mathbf{F}}$  considered as fixed and look for solution in terms of  $\tilde{\mathbf{F}}$ . A linearization of this equation with respect to  $\tilde{\mathbf{F}}^{[n]}$  at step  $n$  gives

$$\mathbb{G} * \left[ \frac{\partial \mathbf{P}}{\partial \mathbf{F}}(\mathbf{F}^{[n]}) : \Delta \tilde{\mathbf{F}}^{[n]} \right] = -\mathbb{G} * \mathbf{P}^{[n]},$$

where we have used  $\mathbf{F}^{[n]} = \bar{\mathbf{F}} + \tilde{\mathbf{F}}^{[n]}$  and  $\mathbf{P}^{[n]} = \partial_{\mathbf{F}}\psi(\bar{\mathbf{F}} + \tilde{\mathbf{F}}^{[n]})$ . Because  $\mathbb{G}$  is numerically explicit in the Fourier space, this equation should be evaluated in the Fourier space and then mapped back to the physical space. To sum up, we obtain the iterative scheme

$$\begin{aligned} \mathcal{F}^{-1} \left\{ \hat{\mathbb{G}} : \mathcal{F} \left[ \frac{\partial \mathbf{P}}{\partial \mathbf{F}}(\mathbf{F}^{[n]}) : \Delta \tilde{\mathbf{F}}^{[n]} \right] \right\} &= -\mathcal{F}^{-1} \left\{ \hat{\mathbb{G}} : \mathcal{F}(\mathbf{P}^{[n]}) \right\}, \\ \tilde{\mathbf{F}}^{[n+1]} &= \tilde{\mathbf{F}}^{[n]} + \Delta \tilde{\mathbf{F}}^{[n+1]}, \end{aligned} \quad (30)$$

where  $\mathcal{F}$  and  $\mathcal{F}^{-1}$  denote the discrete Fourier transform (DFT) and its inverse transform, also called the inverse DFT. The initial guess  $\tilde{\mathbf{F}}^{[0]}$  can be chosen so that its volume average vanishes, that is  $\langle \tilde{\mathbf{F}}^{[0]} \rangle_{\mathcal{R}} = \mathbf{0}$ . Accordingly, we need to apply the following boundary condition at each iteration

$$\langle \tilde{\mathbf{F}}^{[n]} \rangle_{\mathcal{R}} = \mathbf{0} \quad \Leftrightarrow \quad \langle \Delta \tilde{\mathbf{F}}^{[n]} \rangle_{\mathcal{R}} = \mathbf{0} \quad \forall n.$$

Enforcement of this condition has been done by setting the Green operator to be zero at the zero wavenumbers as defined in Equation (28).

### 3.3.2 | Computation of macroscopic tangent moduli

The microscopic BVPs essentially characterize the constitutive law at the macroscale (see also arguments in Section 4.1). In this spirit, we must be able to compute the macroscopic tangent moduli resorting to the information at the microscale. To this end, we pursue the strategy outlined in Rambauck et al<sup>31</sup> and briefly derive the formulation for macroscopic tangent moduli. According to Equation (8), we can compute

$$\bar{\mathbb{C}} = \frac{\partial \bar{\mathbf{P}}}{\partial \bar{\mathbf{F}}} = \frac{1}{|\mathcal{R}|} \int_{\mathcal{R}} \left[ \frac{\partial \mathbf{P}}{\partial \mathbf{F}} : \left( \mathbb{I} + \frac{\partial \tilde{\mathbf{F}}}{\partial \bar{\mathbf{F}}} \right) \right] dV = \left\langle \frac{\partial \mathbf{P}}{\partial \mathbf{F}} : \left( \mathbb{I} + \frac{\partial \tilde{\mathbf{F}}}{\partial \bar{\mathbf{F}}} \right) \right\rangle_{\mathcal{R}}, \quad (31)$$

where  $\mathbb{I}$  is the fourth-order identity tensor. In this equation, the deformation gradient  $\mathbf{F}$  must be obtained as the solution of the microscopic BVP. Thus, it remains to determine the sensitivity of the fluctuation field  $\tilde{\mathbf{F}}$  with respect to the macroscopic field  $\bar{\mathbf{F}}$ , which is also called fluctuation sensitivity (see Miehe et al<sup>14</sup>). These quantities will be revealed by differentiating Equation (29) with respect to  $\bar{\mathbf{F}}$  with the help of decomposition  $\mathbf{F} = \bar{\mathbf{F}} + \tilde{\mathbf{F}}$ . In doing so, we arrive at

$$\mathbb{G} * \left[ \frac{\partial \mathbf{P}}{\partial \mathbf{F}} : \left( \mathbb{I} + \frac{\partial \tilde{\mathbf{F}}}{\partial \bar{\mathbf{F}}} \right) \right] = \mathbf{0} \quad \Leftrightarrow \quad \mathbb{G} * \left( \frac{\partial \mathbf{P}}{\partial \mathbf{F}} : \frac{\partial \tilde{\mathbf{F}}}{\partial \bar{\mathbf{F}}} \right) = -\mathbb{G} * \frac{\partial \mathbf{P}}{\partial \bar{\mathbf{F}}}, \quad (32)$$

where the derivative  $\partial \mathbf{P} / \partial \mathbf{F}$  can be determined because  $\mathbf{F}$  is understood as given by the solution of Equation (29). Obviously, this is a linear system for the fluctuation sensitivity because it is derived from a linearization of Equation (29). Equation (32) can be solved by the conjugate gradient (CG) method acting on the form

$$\mathcal{F}^{-1} \left\{ \hat{\mathbb{G}} : \mathcal{F} \left( \frac{\partial \mathbf{P}}{\partial \mathbf{F}} : \frac{\partial \tilde{\mathbf{F}}}{\partial \bar{\mathbf{F}}} \right) \right\} = -\mathcal{F}^{-1} \left( \hat{\mathbb{G}} : \mathcal{F} \left[ \frac{\partial \mathbf{P}}{\partial \bar{\mathbf{F}}} \right] \right).$$

The CG method is used for solving Equation (32) for two reasons. (i) It is not easy to construct the matrix form of Equation (29) as  $\mathbb{G}$  is only available in the Fourier space. (ii) The left-hand side of this equation is conveniently computed in a componentwise manner and the CG method can be applied to each component of equation.

Since the latter equation is derived from Equation (29), it is essential to pass the average condition associated with Equation (29) on to this equation. Taking derivative of  $\langle \tilde{\mathbf{F}} \rangle = \mathbf{0}$  with respect to  $\bar{\mathbf{F}}$ , the average condition on the fluctuation sensitivity is revealed as follows

$$\left\langle \frac{\partial \tilde{\mathbf{F}}}{\partial \bar{\mathbf{F}}} \right\rangle_{\mathcal{R}} = \mathbf{0}.$$

In the present work, we will call numerical solutions of microscopic BVPs obtained by using the FFT-based high-fidelity solutions. This terminology will be frequently used in Section 5.

## 4 | SURROGATE MODEL USING APPROXIMATOR OF MACROENERGY DENSITY BASED ON NEURAL NETWORKS

### 4.1 | Rationale toward determination of the macroscopic constitutive law with a feedforward neural network

The theory of first-order periodic homogenization basically provides a macroscopic constitutive law in a numerical basis. This statement is reflected by two variational problems (10) and (11). The first variational problem defines the macroscopic energy density without using the given externally applied conditions such as  $\mathbf{f}$  and  $\mathbf{T}$ , while the second problem is characterized by this energy density. A numerical solution of the minimization problem (11) based on gradient-based techniques such as Newton method would require evaluation of the derivatives of  $\bar{\psi}$  (see de Borst et al<sup>39</sup>). In a finite element procedure, such derivatives are only inquired at the quadrature points of the entire problem domain. Therefore, a two-scale computational procedure is laid out as follows: The inquiries of the solver for the macroscopic BVP (11) at one quadrature point are supplied by resolving the corresponding microscopic BVP with the inputs obtained from the solver at the macroscale. We call such procedure a concurrent computational framework.

There are two drawbacks in a concurrent strategy. (i) It is computationally expensive. (ii) The constitutive law is only available at the running time and lost after the computational procedure completes. However, because the constitutive law is associated with the microstructures, or RVEs, of the material, it can be stored and reused in the future applications. The surrogate model arises as a remedy of these advantages. The possibility of constructing the energy density  $\bar{\psi}(\bar{\mathbf{F}})$  by using the material data  $\{(\bar{\mathbf{F}}^{(i)}, \bar{\psi}^{(i)})\}_{i=1}^{N_{\text{data}}}$  is desirable.

Note also that the two-scale computational procedure is not a unique way to achieve the homogenized solution. Indeed, the most fundamental assumption is that we may replace the original problem by the homogenized problem characterized by (10) and (11). This results in the macrohomogeneity condition (5) that should be solved with (10) and (11) to link the micro- and macroscopic quantities. These three equations constitute of an underdetermined system. The macrohomogeneity condition can be fulfilled a priori by applying one of the three boundary conditions in the microscopic BVP or combination of such type of different boundary sections. In doing so, we have plenty of possibilities of solving the microscopic BVPs depending on the means of computing macroscopic energy density. According to this analysis, it is fair to interpret that there are certain amount of noise in the sampling data. This argument is also a strong reinforcement to why we may use neural networks as a sort of interpolation of the macroenergy density.

#### 4.1.1 | Interpretation and terminology

In the current approach, the macroenergy density will be made numerically available by means of a neural network trained on the input-output data collected in the form  $(\bar{\mathbf{F}}, \bar{\psi})$ . The process of collecting data is conducted by solving many microscopic BVPs with given values  $\bar{\mathbf{F}}$  as the inputs and computing the resultant macroenergy density (4) as the outputs. While such a process is called *offline stage*, solving the macroscopic BVP (11) using the approximate macroenergy density is called *online stage*. In combination, these two stages constitute a surrogate model whose overall picture could be recapitulated in Figure 2.

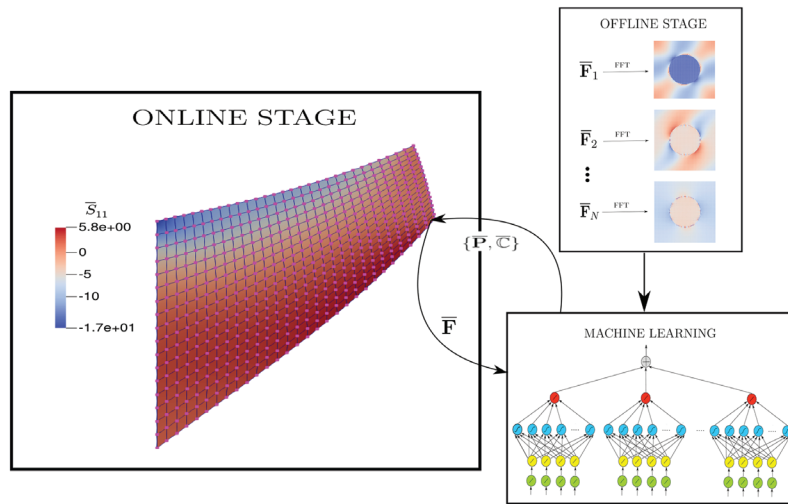


**FIGURE 2** Surrogate model for computational homogenization by means of approximator of macroenergy density

## 4.2 | HDMR-based neural networks

The neural networks employed in this work stems from the contribution of Manzhos and Carrington<sup>38</sup> that embedded partially the structure of high-dimensional model representation (HDMR) into neural networks (NNs). In fact, the above authors aimed at building multidimensional potential energy surfaces, which frequently arise in the field of computational chemistry. An efficient implementation of neural networks with such specific architecture can be found in Manzhos et al.<sup>45</sup>

### 4.2.1 | High-dimensional model representation

A function  $f$  of multivariable  $\mathbf{x} \in [0, 1]^D$  can be approximated by the expansion (cf Manzhos and Carrington<sup>38</sup>)

$$f^{\text{HDMR}}(\mathbf{x}) = f_0 + \sum_{i=1}^D \underbrace{f_i^{(1)}(x_i)}_{\text{component function}} + \sum_{1 \leq i < j \leq D} \underbrace{f_{ij}^{(2)}(x_i, x_j) + \dots + f_{12 \dots D}^{(D)}(x_1, \dots, x_D)}_{\text{mode term}}, \quad (33)$$

which is called a high-dimensional model representation. This expansion consists of a sum of mode terms, each of which is in turn a sum of component functions  $f_{i_1, \dots, i_n}(x_{i_1}, \dots, x_{i_n})$ . In general, a HDMR approximation is achieved by a least-squared optimization problem

$$\min \int_{\mathbb{R}^D} [f(\mathbf{x}) - f^{\text{HDMR}}(\mathbf{x})]^2 d\boldsymbol{\mu}(\mathbf{x}), \quad (34)$$

where  $d\boldsymbol{\mu}$  stands for a predefined measure (see Stein and Shakarchi<sup>46</sup>). Several methods have been proposed by choosing different measures  $d\boldsymbol{\mu}$  and the associated strategies were developed for determining the component functions.

As long as the functional form of the component functions characterized by controlling parameters and the measures  $d\boldsymbol{\mu}$  are defined a priori, the minimization problem (34) can be solved by a suitable gradient-based method. Among all possibilities, using neural networks as component functions is attractive because the functions they represent are universal approximators and efficient methods for computing the network weights are available.

### 4.2.2 | Neural networks based on the structure of high-dimensional representation model

We summarize here the neural networks introduced by Manzhos et al.<sup>45</sup> Then, we adapt the presented theory to our specific application. A theory of artificial neural networks can be found in the standard text by Goodfellow et al.<sup>47</sup>

We recall that a multilayer perceptron (MLP) belongs to the class of feedforward neural networks. It consists of (i) an input layer, (ii) many hidden layers, and (iii) an output layer. The construction of HDMR expansion described below is based on the sum of many MLPs. As for our application, the input layer corresponds to the components of the macroscopic deformation gradient and the output layer to the macroenergy density. Except for the input nodes, each node is a neuron characterized by an associated activation function and its weight and bias parameters. First, we use an Ansatz for the HDMR function  $f^{\text{HDMR}}$  in the form

$$f^{\text{HDMR}}(x_1, \dots, x_D) = \sum_{i=1}^L g_i^{\text{NN}}(\mathbf{x}), \tag{35}$$

where  $D$  is the original number of dimensions and each  $g_i^{\text{NN}}(\mathbf{x})$  is a neural network and there are  $L$  component functions in this expansion. As compared with expression (33), the expansion into multiple mode terms have been imitated at this step. Next, we perform dimensionality reduction in the arguments of  $g_i^{\text{NN}}$  in such a way that

$$g_i^{\text{NN}}(x_1, \dots, x_D) = f_i^{\text{NN}}(y_1^i, y_2^i, \dots, y_d^i), \tag{36}$$

where  $d < D$  is the reduced dimension and the reduced coordinates  $\mathbf{y}^i$  are obtained from the linear mappings

$$\mathbf{y}^i = \mathbf{A}^i \cdot \mathbf{x} + \mathbf{b}^i. \tag{37}$$

where  $\mathbf{A}^i$  is a matrix of size  $(d \times D)$ . At this step, the partial spirit of dimensionality reduction in the component functions of the HDMR expansion (33) has been copied. Now that we employ the feedforward neural network with one hidden single-layer to represent  $f_i^{\text{NN}}$  as follows

$$f_i^{\text{NN}}(y_1^i, \dots, y_d^i) = \sum_{n=1}^{N^i} c_n^i \sigma(\mathbf{w}_n^i \cdot \mathbf{y}^i + v_n^i) + v_0^i, \tag{38}$$

where  $\sigma$  is the activation function for the hidden layer,  $N^i$  is the number of hidden neurons corresponding to the  $i$ th component function. The specific activation function will be presented later for a direct relevance.

Combining Equations (35)-(38), we arrive at

$$f^{\text{HDMR}}(x_1, \dots, x_D) = \sum_{i=1}^L \left\{ \sum_{n=1}^{N^i} c_n^i \sigma^i(\mathbf{w}_n^i \cdot [\mathbf{A}^i \cdot \mathbf{x} + \mathbf{b}^i] + v_n^i) + v_0^i \right\}. \tag{39}$$

In doing so, we actually use  $L$  neural networks with two hidden layers, first of which uses linear activation function while the second uses the nonlinear activation function  $\sigma$ . The ultimate output  $f^{\text{HDMR}}$  is the sum of outputs of all the networks. In Figure 3, the architecture of the overall network (39) is presented.

Note that the function form (39) already reflects the HDMR expansion (33) even though  $d$  is chosen to be identical for all component functions. In fact, if we restrict some rows of  $\mathbf{A}^i$  to be zero, then the components of  $\mathbf{y}^i$  corresponding to these rows will vanish. Nevertheless, it is unnecessary to completely obey the expansion form (33) in minimizing the functional (34) for our applications.

### 4.2.3 | Training of the neural networks for the approximation of macroenergy density

An appropriate measure  $d\mu$  can be chosen so that the functional defined in (34) can be reduced to the arithmetic average of  $(f - f^{\text{HDMR}})^2$  evaluated at all the input data. We recall that such input data are the macroscopic deformation gradient  $\bar{\mathbf{F}}$  and the output data are the corresponding macroenergy density as the outcome of solving the microscopic BVPs. So we need to minimize

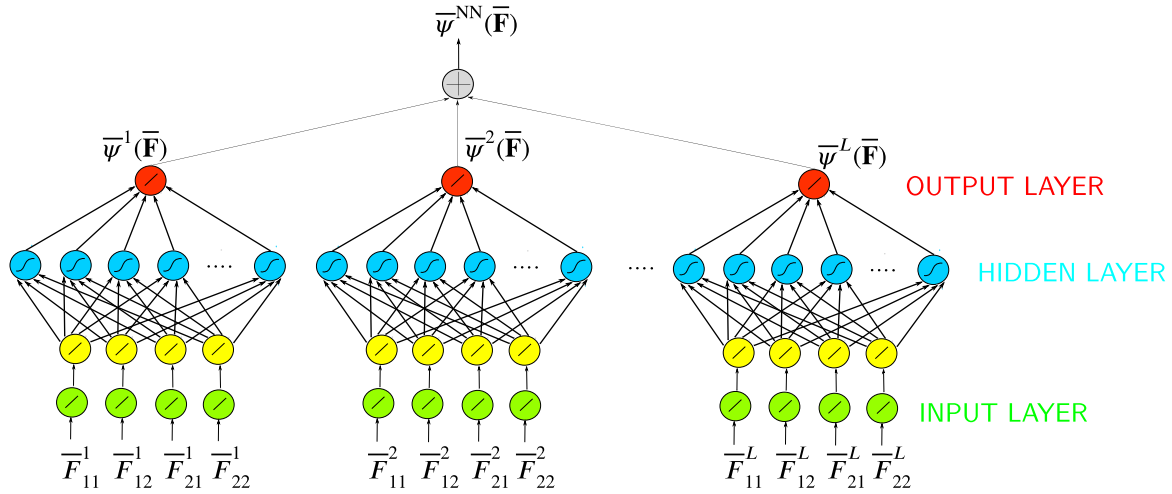


**FIGURE 3** Architecture of the HDMR-based neural network function. A function  $f$  of multidimensional variable  $(x_1, \dots, x_D)$  is approximated by a summation of  $L$  component functions. One component is a neural network with two hidden layers that uses in order the linear activation functions and tanh activation functions. It should be interpreted that  $\bar{F}_{ij}^k = \bar{F}_{ij}$  for all the component functions [Colour figure can be viewed at [wileyonlinelibrary.com](http://wileyonlinelibrary.com)]

$$\frac{1}{|D|} \sum_{\bar{\mathbf{F}} \in D} [\bar{\psi}_{|\bar{\mathbf{F}}} - \bar{\psi}^{\text{NN}}(\bar{\mathbf{F}})]^2 \rightarrow \min \quad (40)$$

with respect to the neuron weights, where  $|D|$  denotes the number of data in  $D$ . In this formulation,  $\bar{\psi}^{\text{NN}}$  is the approximator of the analytical macroenergy density  $\bar{\psi} = \bar{\psi}(\bar{\mathbf{F}})$  and  $\bar{\psi}_{|\bar{\mathbf{F}}}$  is the output data. The explicit expression of  $\bar{\psi}^{\text{NN}}$  is given as in Equation (39) with  $\mathbf{x}$  being replaced with  $\bar{\mathbf{F}}$ . For completeness, we write down the outcome of training process by repeating Equation (39) as follows

$$\bar{\psi}^{\text{NN}}(\bar{\mathbf{F}}) = \sum_{i=1}^L \left\{ \sum_{n=1}^{N^i} c_n^i \sigma^i(\mathbf{w}_n^i \cdot [\mathbf{A}^i \cdot \bar{\mathbf{F}} + \mathbf{b}^i] + v_n^i) + v_0^i \right\}. \quad (41)$$

### 4.3 | Analytical derivatives of neural networks

#### 4.3.1 | Computation of macroscopic stresses and tangent moduli

The finite element method will be used in tandem with the Newton-Raphson method to solve the macroscopic boundary value problem. We briefly go through some important formulas used in our iteration scheme.

The variational equation derived from the minimization problem (11) with  $\bar{\psi}$  replaced by  $\bar{\psi}^{\text{NN}}$  is given by

$$J(\bar{\boldsymbol{\varphi}}, \delta \bar{\boldsymbol{\varphi}}) := \langle D\Pi(\bar{\boldsymbol{\varphi}}), \delta \bar{\boldsymbol{\varphi}} \rangle = \int_B \nabla \delta \bar{\boldsymbol{\varphi}} : \frac{\partial \bar{\psi}^{\text{NN}}}{\partial \bar{\mathbf{F}}} dV - \int_B \mathbf{f} \cdot \delta \bar{\boldsymbol{\varphi}} dV - \int_{\Gamma_N} \mathbf{T} \cdot \delta \bar{\boldsymbol{\varphi}} dA = 0 \quad \forall \delta \bar{\boldsymbol{\varphi}}.$$

Linearization of the left-hand side of the latter equation with respect to  $\bar{\boldsymbol{\varphi}}$  gives

$$\langle DJ(\bar{\boldsymbol{\varphi}}, \delta \bar{\boldsymbol{\varphi}}), \Delta \bar{\boldsymbol{\varphi}} \rangle = \int_B \delta \bar{\mathbf{F}} : \frac{\partial^2 \bar{\psi}^{\text{NN}}}{\partial \bar{\mathbf{F}} \partial \bar{\mathbf{F}}} : \Delta \bar{\mathbf{F}} dV.$$

Then, the Newton-Raphson iteration is formulated as



$$\begin{aligned} \langle DJ(\bar{\boldsymbol{\varphi}}^{[k]}, \delta\bar{\boldsymbol{\varphi}}), \Delta\bar{\boldsymbol{\varphi}}^{[k]} \rangle &= \langle \mathbf{f}, \delta\bar{\boldsymbol{\varphi}} \rangle + \langle \bar{\mathbf{t}}, \delta\bar{\boldsymbol{\varphi}} \rangle_{\Gamma_N} - \langle \bar{\mathbf{P}}^{\text{NN},[k]}, \delta\bar{\mathbf{F}} \rangle \quad \forall \delta\bar{\boldsymbol{\varphi}}, \\ \bar{\boldsymbol{\varphi}}^{[k+1]} &= \bar{\boldsymbol{\varphi}}^{[k]} + \Delta\bar{\boldsymbol{\varphi}}^{[k]}, \end{aligned} \quad (42)$$

where we have used the following inner product notations

$$\langle \bar{\mathbf{P}}^{\text{NN},[k]}, \delta\bar{\mathbf{F}} \rangle = \int_B \partial_{\bar{\mathbf{F}}} \bar{\psi}^{\text{NN}}(\bar{\mathbf{F}}^{[k]}) : \nabla \delta\bar{\boldsymbol{\varphi}} \, dV, \quad \langle \mathbf{f}, \delta\bar{\boldsymbol{\varphi}} \rangle = \int_B \mathbf{f} \cdot \delta\bar{\boldsymbol{\varphi}} \, dV, \quad \langle \mathbf{T}, \delta\bar{\boldsymbol{\varphi}} \rangle_{\Gamma_N} = \int_{\Gamma_N} \mathbf{T} \cdot \delta\bar{\boldsymbol{\varphi}} \, dA.$$

At each iteration of the algorithm (42), we need to compute the stress and the tangent stiffness as follows

$$\bar{\mathbf{P}}^{\text{NN}} = \frac{\partial \bar{\psi}^{\text{NN}}}{\partial \bar{\mathbf{F}}}, \quad \bar{\mathbb{C}}^{\text{NN}} = \frac{\partial^2 \bar{\psi}^{\text{NN}}}{\partial \bar{\mathbf{F}} \partial \bar{\mathbf{F}}}.$$

In the present work, we exclusively use the tanh as the activation function, that is,  $\sigma^i(x) = \sigma(x) = \tanh(x)$  for all activation functions, which implies

$$\sigma'(x) = 1 - \sigma(x)^2, \quad \sigma''(x) = 2\sigma(x)[\sigma(x)^2 - 1].$$

Taking the first and second derivatives of expression (41) with respect to  $\bar{\mathbf{F}}$ , we arrive at

$$\begin{aligned} \bar{\mathbf{P}}^{\text{NN}} &= \sum_{i=1}^L \left\{ \sum_{n=1}^{N^i} c_n^i \mathbf{w}_n^i \cdot \mathbf{A}^i [1 - \sigma(q^i)^2] \right\}, \quad \text{with } q^i = \mathbf{w}_n^i \cdot [\mathbf{A}^i \cdot \bar{\mathbf{F}} + \mathbf{b}^i] + v_n^i, \\ \bar{\mathbb{C}}^{\text{NN}} &= \sum_{i=1}^L \left\{ \sum_{n=1}^{N^i} 2c_n^i (\mathbf{w}_n^i \cdot \mathbf{A}^i)^T \cdot (\mathbf{w}_n^i \cdot \mathbf{A}^i) [\sigma(q^i)^2 - 1] \sigma(q^i) \right\}. \end{aligned} \quad (43)$$

These two expressions are the approximators of  $\bar{\mathbf{P}}$  and  $\bar{\mathbb{C}}$  that will be used in the macroscopic solver.

### 4.3.2 | Feature normalization and recover to the physical values

In this part, we draw special attention to one crucial practice in implementation for those who wish to use the package provided in Manzhos et al.<sup>45</sup> As standardized in MATLAB package and many existing libraries, the training process of neural networks accepts the normalized features, including inputs and outputs, to accelerate the convergence of the algorithm. This step of feature normalization must be taken into account for our implementation.

We borrow again the representation (39) to illustrate the feature normalization step. Let us assume that the range of the input coordinates and the output coordinates are respectively given by

$$\begin{aligned} \Omega_r^{\text{input}} &= [(x_r)_{\min}, (x_r)_{\max}], & (x_r)_{\min} &= \min \{(x_r)_j\}_{j=1}^{N_{\text{data}}}, & (x_r)_{\max} &= \max \{(x_r)_j\}_{j=1}^{N_{\text{data}}}, \\ \Omega^{\text{output}} &= [f_{\min}, f_{\max}], & f_{\min} &= \min \{f_j\}_{j=1}^{N_{\text{data}}}, & f_{\max} &= \max \{f_j\}_{j=1}^{N_{\text{data}}}, \end{aligned} \quad (44)$$

in which  $(x_r)_{\min}, (x_r)_{\max}$  means the minimum and maximum of the input data in  $r$ -direction, with  $1 \leq r \leq D$ , and  $f_{\min}$  and  $f_{\max}$  are the minimum and maximum of the output data. The input and output data are both normalized to the range  $[-1, 1]$  by the following scaling

$$(\xi_r)_j = 2 \frac{(x_r)_j - (x_r)_{\min}}{(x_r)_{\max} - (x_r)_{\min}} - 1, \quad g_j = 2 \frac{f_j - f_{\min}}{f_{\max} - f_{\min}} - 1, \quad \forall r = 1, \dots, D, \quad (45)$$

where  $\xi_j$  and  $g_j$  are the scaled data. Following the definitions of the min- and max-quantities given in Equation (44), it is evident that  $(x_r)_j \in [-1, 1]$  and  $g_j \in [-1, 1]$ .

Assume that  $f^{\text{HDMM}}(\mathbf{x})$  is trained from the original data  $D = \{\mathbf{x}_j, f_j\}_{j=1}^{N_{\text{data}}}$  and similarly  $g^{\text{HDMM}}(\xi)$  from the normalized data  $D_{\text{norm}} = \{\xi_j, g_j\}_{j=1}^{N_{\text{data}}}$ . These two neural network functions are related to each other by a transformation that is the *continuous* version of data scaling (45). Concretely, the transformation is given as follows

$$f^{\text{HDMM}}(\mathbf{x}) = \frac{\Delta f}{2} [g^{\text{HDMM}}(\xi(\mathbf{x})) + 1] + f_{\min}, \quad \xi_r = 2 \frac{x_r - (x_r)_{\min}}{\Delta x_r} - 1,$$

where  $\Delta f = f_{\max} - f_{\min}$  and  $\Delta x_r = (x_r)_{\max} - (x_r)_{\min}$ .

Now, note that the package given in Manzhos et al<sup>45</sup> accepts the normalized data  $D_{\text{norm}}$  and generates  $g^{\text{HDMM}}$  in terms of the associated neural network weights. Therefore, to compute the derivative of  $f^{\text{HDMM}}$  with respect to the *original* coordinate  $\mathbf{x}$ , we rely on the chain rule

$$\frac{\partial}{\partial x_r} f^{\text{HDMM}} = \frac{\Delta f}{2} \left[ \sum_{s=1}^D \frac{\partial g^{\text{HDMM}}}{\partial \xi_s} \frac{2}{\Delta x_s} \delta_{sr} \right] = \frac{\Delta f}{\Delta x_r} \frac{\partial}{\partial \xi_r} g^{\text{HDMM}} \quad \forall r = 1, \dots, D.$$

The first derivative serves for computation of the macroscopic stresses (43)<sub>1</sub>. Similarly, the second derivative

$$\frac{\partial^2}{\partial x_r \partial x_s} f^{\text{HDMM}} = \frac{\Delta f}{\Delta x_r \Delta x_s} \frac{\partial^2}{\partial \xi_r \partial \xi_s} g^{\text{HDMM}} \quad \forall r, s = 1, \dots, D$$

is employed for computation of the macroscopic tangent moduli (43)<sub>2</sub>.

## 5 | REPRESENTATIVE NUMERICAL EXAMPLES

The examples are chosen to demonstrate the robustness of the proposed computational framework, and they are presented in the order of difficulty. To gain confidence in the reliability of the neural network outcome, that is, macroenergy density, we show in all examples, when relevant, the analytical solution or the full-field solution as a mean of comparison.

We start with a one-dimensional toy problem where the heterogeneity is idealized and mathematically characterized by the energy density with oscillating material parameters. The second and third examples aim at justifying the approximate stress field and tangent moduli given by Equation (43) as compared to the corresponding quantities obtained through the FFT-based solver for microscopic BVP. The last two numerical examples delve into the real-world applications where three types of solutions are constructed for comparison: (i) numerical solution by a surrogate modeling, (ii) numerical solution by a concurrent computational approach, and (iii) full-field solution.

The details regarding the neural network architectures and number of material data used in the below examples are given in Table 2, while the interpretation of the variables in this table are recalled in Table 1. In all the numerical examples, we have used  $d = D$  for all the component functions although different values of  $d$  for different component functions will reflect better the idea of high-dimensional model representation. However, using the same value for  $d$ , the component function with less dependency on certain variables will reduce the corresponding weights in its associated layer. Truncating the HDMM in the approximation, it does not harm by setting  $d = D$  because the computational cost for training is much less than that spent for the data collection process. To prevent the overfitting issue, we split our database into two sets: training data and validation data and use cross-validation in the training procedure. Other methods, such as dropout, regularization, and their applications in computational homogenization have been discussed by Wang and Sun<sup>48</sup>

**TABLE 1** Meanings of the parameters that describe the architecture of neural network (41)

$D$	Original dimension of the variable $\bar{\mathbf{F}}$ as the input argument of $\bar{\psi}$
$d$	Reduced dimension; refer to Equation (36)
$L$	Number of component functions; refer to Equation (41)
$N$	Number of neurons in the second hidden layer of the component function; refer to Equation (38)
$N_{\text{data}}$	Number of data for training the network (39); refer to Equation (34)

**TABLE 2** Record of architectures of neural networks used in our numerical examples

Examples	$D$	$d$	$L$	$N$	$N_{\text{data}}$
Example 5.1	1	1	2	5	$10^3$
Example 5.2	4	4	15	20	$50 \times 10^3$
Example 5.3	4	4	15	20	$30 \times 10^3$

Note: The meaning of these variables are defined in Table 1.

(see also Srivastava et al<sup>49</sup>). Furthermore, we have increased the hyperparameters  $L$  and  $N$  from rather small numbers step by step to upgrade the complexity of the neural network. The hyperparameters are finally chosen so that the network can perform well on the validation set and thus approximate the macroenergy density with high accuracy.

## 5.1 | A mathematical one-dimensional toy problem

Let us start with a simple bar problem described by the following minimization problem (see Figure 4)

$$\delta \left\{ \int_0^L \psi(X, \epsilon) \, dX - \int_0^L f(X) u(X) \, dX - [\bar{t}_0 u(X)]_{X=L} \right\} = 0, \quad \psi(X, \epsilon) = \mu(X) \left[ \frac{2}{3}(1 + \epsilon)^{3/2} - \epsilon - \frac{2}{3} \right]$$

with the essential boundary condition  $u(0) = 0$ . Note that  $\psi(X, \epsilon = 0) = 0$ . In this formulation,  $X$  is the reference coordinate,  $t_0$  is the traction force applied to the bar at  $X = L$ , with  $L = 1$ ,  $\epsilon = du/dX$  denotes the gradient of the displacement field, and the mathematical parameter  $\mu = \mu(X)$  representing the inhomogeneities is given by

$$\mu(X) = \frac{3}{2} + \sin(2\pi kX), \quad k \in \mathbb{Z}^+.$$

This boundary value problem in the strong form reads

$$\frac{d}{dX} \frac{\partial \psi}{\partial \epsilon} + f(X) = 0,$$

where the boundary conditions are translated to

$$u(0) = 0, \quad \frac{\partial \psi}{\partial \epsilon} \left( X \rightarrow L, \epsilon \rightarrow \frac{du}{dX}(L) \right) = t_0.$$

The RVE is depicted by  $\mu(\xi)$  on one wavelength  $1/k$ , that is  $\mu(\xi)$  defined on the interval  $\xi \in (X - 1/2k, X + 1/2k)$ . The microscopic BVPs are solved for  $10^3$  input macroscopic strain data  $\bar{\epsilon}$  that are randomly distributed in the range  $[0, 2]$  to compute the output data of macroenergy density. As the microscopic BVPs can be solved analytically as in Nguyen et al,<sup>50</sup> the material data can be easily collected. Thus, we used  $10^3$  data points for the high resolution of the macroscopic solution, although much less data could provide high-quality solution. The approximate energy density  $\bar{\psi}^{\text{NN}}$  is obtained by using two component functions, each of which has five neurons in its second hidden layer (see row Example 5.1 of Table 2). In Figure 5, the homogenized solutions obtained by the surrogate model and a concurrent approach are compared with the full-field solutions obtained with different wavenumber values  $k$ . We see that when  $k \rightarrow \infty$ , the full-field solution converges to the homogenized solution. In addition, the surrogate-modeling solution agrees excellently with the concurrent-modeling solution.

## 5.2 | Surrogate model for a laminate microstructure

### 5.2.1 | Problem setting

In this section, we study a two-dimensional homogenization problem, which accepts an analytical solution. Particularly, we analyze a two-dimensional laminate RVE in the plane strain condition (see Figure 6). This RVE comprises two phases

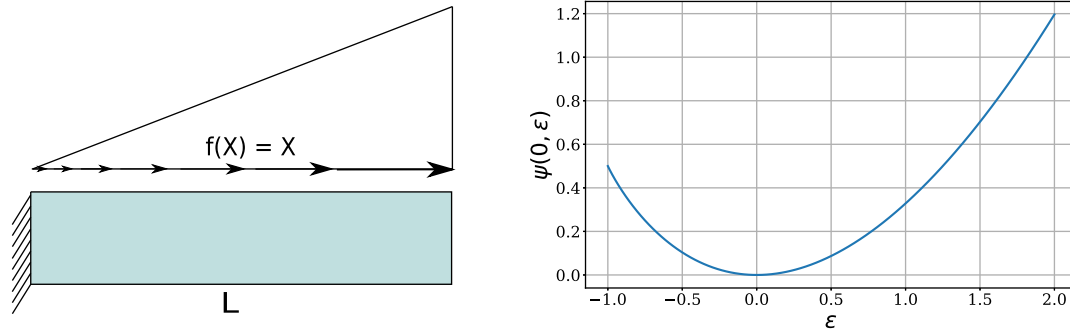


**FIGURE 4** Mathematical toy problem. (Left) Problem setting of the mathematical heterogeneous bar subject to a traction. (Right) With  $\mu(0) = 3/2$ , the energy function  $\psi(0, \epsilon) = (1 + \epsilon)^{3/2} - 3/2\epsilon - 1$  is plotted against the  $\epsilon$ -coordinate [Colour figure can be viewed at [wileyonlinelibrary.com](http://wileyonlinelibrary.com)]

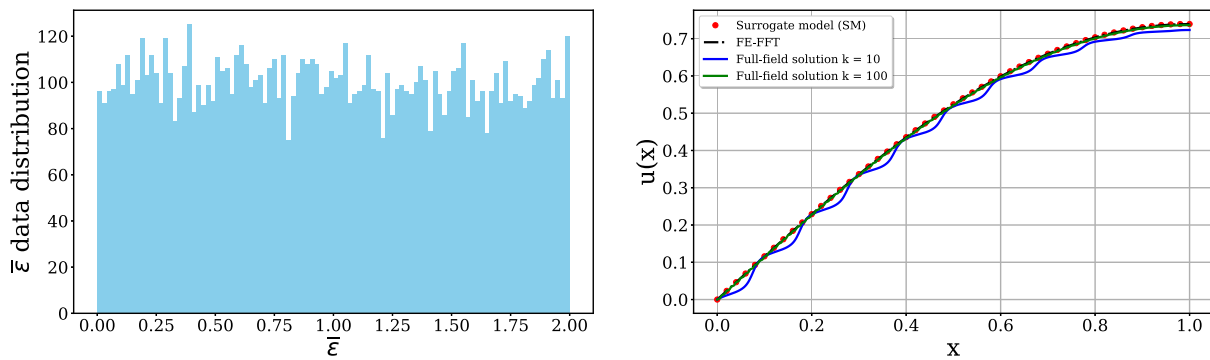


**FIGURE 5** Comparison between homogenization solution and full-field solution. (Left) The 100 macroscopic strain data  $\bar{\epsilon}$  is uniformly distributed in the range  $[0,2]$  and shown by its histogram plot. (Right) The homogenized solution is obtained by using the neural network macroenergy density (red dots) with 1000 sampling data and by the concurrent FE-FFT method (black dashed line). The full-field solutions corresponding to  $k = 10$  and  $k = 100$  (blue and green curves) are obtained by using standard FEM with a high number of elements [Colour figure can be viewed at [wileyonlinelibrary.com](http://wileyonlinelibrary.com)]

of Neo-Hookean material

$$\psi(\mathbf{F}) = \frac{\mu}{2}[\text{trace}(\mathbf{F}^T \cdot \mathbf{F}) - 2] + \frac{\mu}{\beta}[\det(\mathbf{F})^{-\beta} - 1],$$

where  $\mu$  is the shear modulus and  $\beta$  is determined in terms of Poisson ratio  $\nu$  according to  $\beta = 2\nu/(1 - \nu)$ . The gradient and hessian of  $\psi(\mathbf{F})$  are the stress tensor and tangent moduli that are explicitly computed as follows

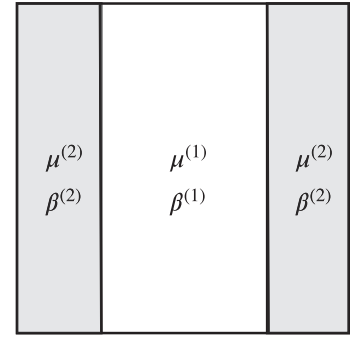
$$P_{ij} = \frac{\partial \psi}{\partial F_{ij}} = \mu F_{ij} - \mu \det(\mathbf{F})^{-\beta} F_{ji}^{-1},$$

$$C_{ijkl} = \frac{\partial^2 \psi}{\partial F_{kl} \partial F_{ij}} = \mu \delta_{ik} \delta_{jl} + \mu \det(\mathbf{F})^{-\beta} (\beta F_{ji}^{-1} F_{lk}^{-1} + F_{jk}^{-1} F_{li}^{-1}),$$

where  $\mathbf{F}^{-1}$  is the inverse tensor of  $\mathbf{F}$ . We denote by  $(*)^{(i)}$  the material parameter  $(*)$  associated with phase  $\alpha$ ,  $\alpha = 1, 2$  and in this example we consider

$$\mu^{(1)} = 100, \quad \mu^{(2)} = 1000, \quad \text{and} \quad \beta^{(1)} = \beta^{(2)} = 1 \Leftrightarrow \nu^{(1)} = \nu^{(2)} = 1/3.$$

**FIGURE 6** An RVE of laminate structure under plane strain condition. The laminate consists of two phases of Neo-Hookean materials. Each phase takes up 50% volume of the entire RVE



### 5.2.2 | Analytical solution

The microscopic boundary value problem corresponding to the laminate structure above admits an analytical solution. For self-contained reading, we summarize the main steps given in the work Gözüüm et al,<sup>30</sup> which dealt with the laminate RVE problem of the electromechanically coupled materials. We will derive here a system of algebraic equations for determining the gradient deformation fields  $\mathbf{F}^{(i)}$  distributed within two phases, which result from the application of a generic macroscopic deformation gradient  $\bar{\mathbf{F}}$ . First, we recall that the two following differential equations must be fulfilled throughout the RVE

$$\nabla \cdot \mathbf{P}^T = \mathbf{0}, \quad \nabla \times \mathbf{F} = \mathbf{0} \quad \Leftrightarrow \quad P_{ijj} = 0, \quad \epsilon_{imn} F_{jn,m} = 0.$$

The first equation is the equilibrium equation in the RVE domain, while the second is the compatibility condition. For a two-dimensional problem, these equations are

$$\begin{aligned} P_{11,1} + P_{12,2} &= 0, & F_{12,1} - F_{11,2} &= 0, \\ P_{21,1} + P_{22,2} &= 0, & F_{22,1} - F_{21,2} &= 0. \end{aligned}$$

It can be deduced from the assembly of the laminate phases that the variables appearing in the last equations are independent of  $X_2$ . Taking this fact into account, we arrive at

$$\begin{aligned} P_{11,1} &= 0, & P_{21,1} &= 0, \\ F_{12,1} &= 0, & F_{22,1} &= 0. \end{aligned}$$

which implies  $P_{11}, P_{21}, F_{12}, F_{22}$  are all independent of  $X_1$  and  $X_2$ . In short, these fields are constant throughout the entire RVE domain. Due to the laminate structure, all variables  $P_{12}, P_{22}$  and  $F_{11}, F_{21}$  are constant within each phase. Accordingly, it is possible to reuse the notation  $F_{ij}^{(\alpha)}$  and  $P_{ij}^{(\alpha)}$  to denote the scalar values which the components of  $\mathbf{F}$  and  $\mathbf{P}$  take on throughout the phase ( $\alpha$ ).

At this point, we have eight unknowns  $F_{ij}^{(\alpha)}$  with  $i, j = 1, 2, \alpha = 1, 2$ , and four equations

$$\begin{aligned} F_{12}^{(1)} &= F_{12}^{(2)}, & F_{22}^{(1)} &= F_{22}^{(2)}, \\ P_{11}^{(1)} &= P_{11}^{(2)}, & P_{21}^{(1)} &= P_{21}^{(2)}. \end{aligned}$$

The other four equations come from the essential boundary condition of the microscopic BVP. They are the average conditions

$$\frac{1}{|\mathcal{R}|} \int_{\mathcal{R}} F_{ij} \, dV = \bar{F}_{ij} \quad \Leftrightarrow \quad \frac{1}{2} [F_{ij}^{(1)} + F_{ij}^{(2)}] = \bar{F}_{ij}.$$

Keeping in mind that  $\mathbf{P} = \partial_{\mathbf{F}} \psi$  is given in terms of  $\mathbf{F}$ , we have just obtained eight equations for determining the eight unknowns  $F_{ij}^{(\alpha)}$  as follows

$$\begin{aligned}
F_{12}^{(1)} = F_{12}^{(2)} = \bar{F}_{12}, \quad \frac{1}{2}[F_{11}^{(1)} + F_{11}^{(2)}] = \bar{F}_{11}, \quad \frac{\partial \psi^{(1)}}{\partial F_{11}} = \frac{\partial \psi^{(2)}}{\partial F_{11}}, \\
F_{22}^{(1)} = F_{22}^{(2)} = \bar{F}_{22}, \quad \frac{1}{2}[F_{21}^{(1)} + F_{21}^{(2)}] = \bar{F}_{21}, \quad \frac{\partial \psi^{(1)}}{\partial F_{21}} = \frac{\partial \psi^{(2)}}{\partial F_{21}}.
\end{aligned} \tag{46}$$

As long as the variable  $\bar{\mathbf{F}}$  is given,  $\mathbf{F}^{(i)}$  for each phase can be computed with high accuracy. We address the solutions numerically obtained from this nonlinear system of algebraic equations as analytical solutions. Using these solutions, we can compute the macroenergy density according to

$$\bar{\psi}^{\text{analytical}} = \frac{1}{|\mathcal{R}|} \int_{\mathcal{R}} \psi \, dV = \frac{1}{2} [\psi(\mathbf{F}^{(1)}) + \psi(\mathbf{F}^{(2)})]. \tag{47}$$

The exact macroscopic stress is computed as

$$\bar{\mathbf{P}}^{\text{analytical}} = \frac{1}{2} \left[ \frac{\partial \psi}{\partial \mathbf{F}}(\mathbf{F}^{(1)}) + \frac{\partial \psi}{\partial \mathbf{F}}(\mathbf{F}^{(2)}) \right] = \frac{1}{2} [\mathbf{P}^{(1)} + \mathbf{P}^{(2)}]. \tag{48}$$

We use the *central difference* formula with an extremely small perturbation  $\epsilon$  to compute the corresponding “exact” tangent moduli according to

$$\bar{C}_{ijkl}^{\text{analytical}} \approx \frac{\bar{P}_{ij}^{(+)} - \bar{P}_{ij}^{(-)}}{2\epsilon}, \quad \bar{P}_{ij}^{(\pm)} = \bar{P}_{ij}(\bar{\mathbf{F}})_{|\bar{F}_{kl} \rightarrow \bar{F}_{kl} \pm \epsilon}, \tag{49}$$

where  $\bar{P}_{ij}^{(\pm)}$  are computed according to Equation (48) by using the input  $\bar{\mathbf{F}}$  with  $\bar{F}_{kl}$  being replaced by  $\bar{F}_{kl} \pm \epsilon$ . Exact quantities (47)-(49) will be used to compare the numerical solutions obtained by FFT-based approach and neural network surrogate model.

### 5.2.3 | Numerical results

In Figure 7, we show the macroenergy density, the stress component  $\bar{P}_{11}$ , and the tangent moduli component  $\bar{C}_{1111}$ , which are computed from the surrogate model, the high-fidelity solution (FFT-based solution), and the analytical solution (46). As for this comparison, we assemble  $N_{\text{data}} = 50 \times 10^3$  data points extracted from a database of  $200 \times 10^3$  data points  $\bar{F}_{ij}$ , which are uniformly distributed in the range

$$\begin{bmatrix} \bar{F}_{11} & \bar{F}_{12} \\ \bar{F}_{21} & \bar{F}_{22} \end{bmatrix} \because \begin{bmatrix} 0.7 \rightarrow 1.3 & -0.3 \rightarrow 0.3 \\ -0.3 \rightarrow 0.3 & 0.7 \rightarrow 1.3 \end{bmatrix}.$$

We recall that macroscopic deformation gradients and the resulting macroenergy density play the role of input data and output data, respectively. In addition, the architecture of the neural network for this training is defined by the parameters  $L = 15$  and  $N = 20$  as shown in row Example 5.2 of Table 2.

Although we could notice the differences in stress and tangent moduli components, it is yet difficult to see any differences in the macroenergy density. Indeed, it can be observed from Figure 8 that the relative errors in energy provided by the surrogate-model solution and the high-fidelity solution as compared to the exact energy are very small. Hereby, we highlight our argument regarding the obvious differences in the stress field and tangent moduli. At first sight, such differences might lead to an impression that the method generated large approximation error in the solution. However, it is not necessarily true because the minimum point of the approximate macroenergy density is close to the exact counterpart. This reasoning is applicable to the results shown in the first column of Figure 7 and also the ones in subsequent numerical examples.

To further validate the proposed computational framework, we conduct another set of numerical experiments. We study the components of macroscopic stress and tangent moduli by fixing the components  $\bar{F}_{11} = \bar{F}_{22} = 1.2$ ,  $\bar{F}_{21} = -0.2$  and then letting  $\bar{F}_{12}$  to vary arbitrarily in the range  $[-0.2, 0.2]$ . In Figure 9, the multiple components of  $\bar{\mathbf{P}}^{\text{NN}}$  and  $\bar{\mathbf{C}}^{\text{NN}}$  are

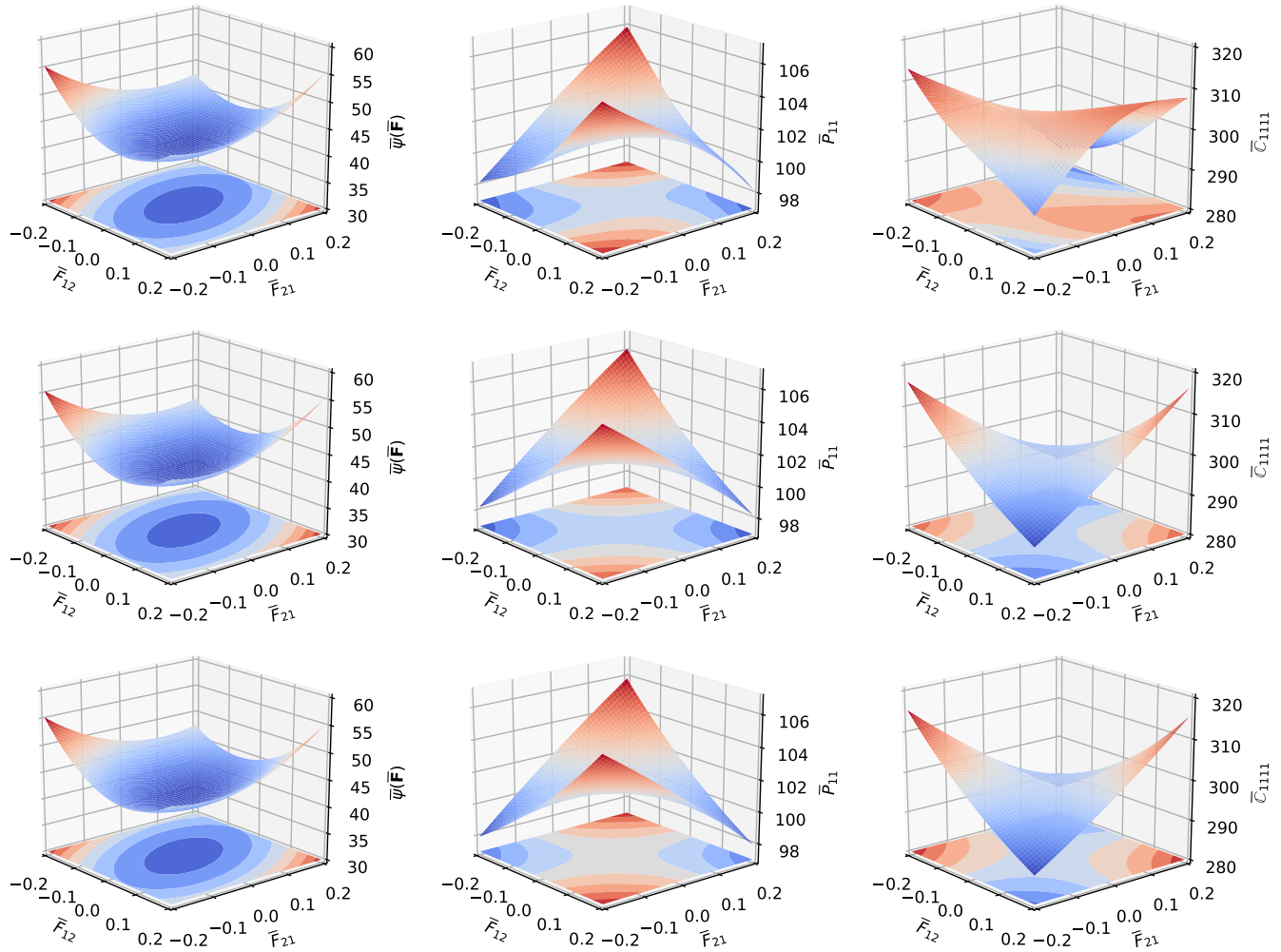


**FIGURE 7** Comparison between surrogate-model solution, high-fidelity solution and analytical solution. The macroscopic energy density (left column), the stress component  $\bar{P}_{11}$  (middle column) and the tangent moduli component  $\bar{C}_{1111}$  (right column) are ordered according to the following navigation: (top row) surrogate-model solution, (middle row) high-fidelity solution and (bottom row) analytical solution. The plots are generated by fixing  $\bar{F}_{11} = \bar{F}_{22} = 1.2$  and varying  $\bar{F}_{12}, \bar{F}_{21}$  in the interval  $[-0.2, 0.2]$  [Colour figure can be viewed at [wileyonlinelibrary.com](http://wileyonlinelibrary.com)]

presented by using  $N_{\text{data}} = 50 \times 10^3$  training data for construction of  $\bar{\psi}^{\text{NN}}$  (see row Example 5.4 of Table 2). The high-fidelity quantities  $\bar{\mathbf{P}}$  and  $\bar{\mathbf{C}}$  are obtained by using the high-fidelity solutions and formulas (8) and (31). The comparison shows that excellent results can be obtained not only by the FFT-based method but also by the neural network approximation. In addition, it reveals that the surrogate model captures the expected anisotropic property of the homogenized material extremely well. This leads us to the next numerical study where analytical solution of the microscopic BVP is not available.

### 5.3 | Surrogate model for a microstructure of circular inclusion

#### 5.3.1 | Problem setting

In this numerical experiment, we study a two-dimensional RVE with circular inclusion in a plane strain analysis. Such RVE is a two-dimensional reduction of the cylindrical inclusion of a three-dimensional RVE with quite large dimension along the axis of the cylinder. We denote the quantities associated with the inclusion and the matrix by the superscripts (i) and (m), respectively. The circular inclusion takes up a volume fraction  $f^{(i)} = 20\%$  and hence its radius is determined by  $\pi[R^{(i)}]^2 = f^{(i)}L_1L_2$ , where  $L_1 = L_2 = 1$  are lengths of the sides of the RVE (see Figure 10).

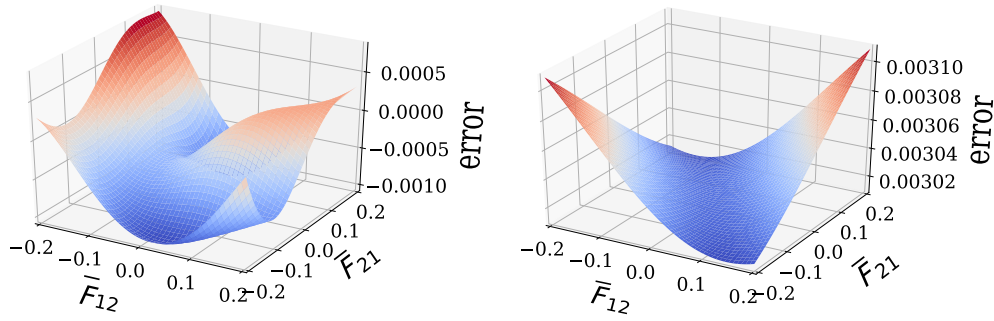


**FIGURE 8** Relative error in macroenergy density. The relative errors in macroenergy density of the surrogate-model solution and the high-fidelity solution as compared the analytical solution are shown on the left and the right figure, respectively. The relative errors are computed by dividing the corresponding absolute errors by the exact macroenergy density [Colour figure can be viewed at [wileyonlinelibrary.com](http://wileyonlinelibrary.com)]

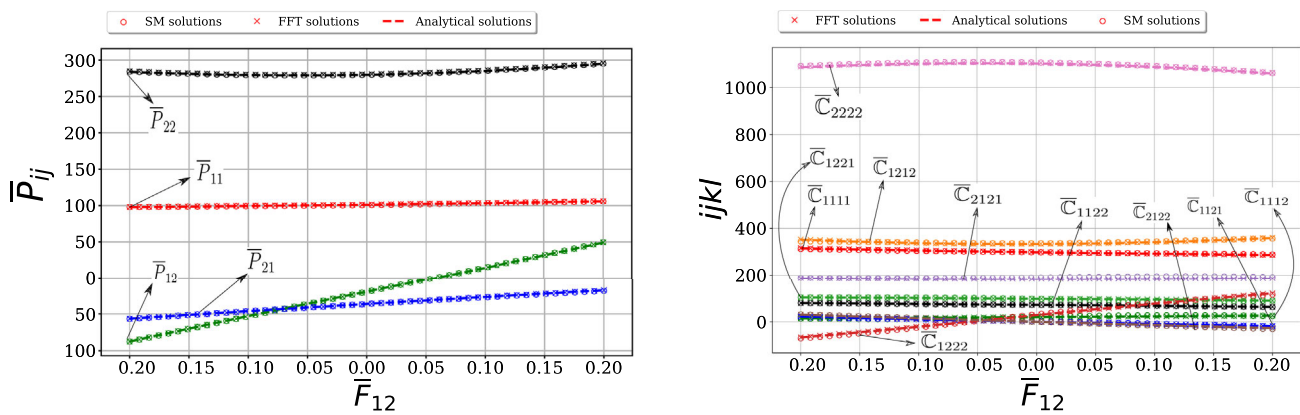


**FIGURE 9** Macroscopic stress  $\bar{\mathbf{P}}$  and tangent moduli  $\bar{\mathbf{C}}$ . The macroscopic stress (left) and tangent moduli (right) are produced by the surrogate model trained on  $50 \times 10^3$  data points. These tensors are compared with the counterparts generated by using the high-fidelity solution and analytical solution. All the numerical results are plotted against the varying component  $\bar{F}_{12} \in [-0.2, 0.2]$ , while other three components  $\bar{F}_{11} = \bar{F}_{22} = 1.2$ , and  $\bar{F}_{21} = -0.2$  are kept fixed [Colour figure can be viewed at [wileyonlinelibrary.com](http://wileyonlinelibrary.com)]

The constituting phases are made of the Neo-Hookean materials characterized by the energy density (cf Yvonnet et al<sup>51</sup>)

$$\psi(\mathbf{C}) = \frac{1}{2} \lambda [\log(J)]^2 - \mu \log(J) + \frac{1}{2} \mu [\text{trace}(\mathbf{C}) - 2], \quad (50)$$

where  $\mathbf{C} = \mathbf{F}^T \cdot \mathbf{F}$  is the right Cauchy stress tensor,  $J = \det(\mathbf{F})$ ,  $\lambda$  and  $\mu$  are the Lamé parameters given in terms of Young modulus  $E$  and Poisson ratio  $\nu$  as follows

$$\lambda = \frac{E\nu}{(1+\nu)(1-2\nu)}, \quad \mu = \frac{E}{2(1+\nu)}.$$

As for our example, we choose

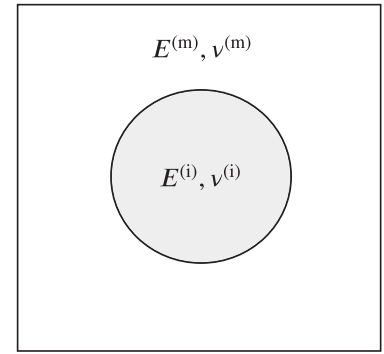
$$E^{(m)} = 100 \text{ MPa}, \quad \nu^{(m)} = 0.4, \quad E^{(i)} = 1000 \text{ MPa}, \quad \nu^{(i)} = 0.3. \quad (51)$$

The stress tensor  $\mathbf{P} = \partial\psi/\partial\mathbf{F}$  and tangent moduli  $\mathbf{C} = \partial^2\psi/\partial\mathbf{F}\partial\mathbf{F}$  are derived as follows

$$P_{ij} = \mu F_{ij} + [\lambda \log(J) - \mu] F_{ji}^{-1},$$



**FIGURE 10** An RVE with circular inclusion. The RVE consists of two phases: (i) a circular inclusion and (m) a matrix surrounding the inclusion. Two phases are made of the Neo-Hookean materials that are characterized by the energy density (50) and the associated Young modulus and Poisson ratio. These material parameters are specialized to each phase



$$C_{ijkl} = \lambda F_{ji}^{-1} F_{lk}^{-1} - [\lambda \log(J) - \mu] F_{jk}^{-1} F_{li}^{-1} + \mu \delta_{ik} \delta_{jl}.$$

### 5.3.2 | Numerical results

In this example, we use a database of  $30 \times 10^3$  uniformly distributed data points in the following range

$$\begin{bmatrix} \bar{F}_{11} & \bar{F}_{12} \\ \bar{F}_{21} & \bar{F}_{22} \end{bmatrix} \because \begin{bmatrix} 0.8 \rightarrow 1.2 & -0.5 \rightarrow 0.5 \\ -0.5 \rightarrow 0.5 & 0.8 \rightarrow 1.2 \end{bmatrix}$$

for training process. Because the analytical solution is not available for this RVE problem, we show in Figure 11 only the numerical results of the macroenergy density  $\bar{\psi}$ , stress field  $\bar{P}_{11}$ , and tangent modulus  $\bar{C}_{1111}$  obtained by the FFT-based and surrogate-model computations. We also note that the solution of the RVE problem contains the spurious ringing artifacts surrounding the material interfaces (see Figure 12). This phenomenon occurs for the microstructure in which the interfaces between phases are not aligned along the orthogonal axes of the mesh. When we refine the mesh, the interpolations of the solution at the grid points in the mesh would not converge uniformly to the classical solution but still converge pointwise. Surprisingly, the spurious oscillations do not appear for microstructures with interfaces aligned with the axes of the mesh (see Zeman et al<sup>33</sup>). Indeed, such artifacts are not observed in the last example investigating the laminate microstructure. Two recent papers by Rovinelli et al<sup>52</sup> and Ma and Sun,<sup>53</sup> among several others, have partly resolved this issue.

Once again, we have fixed  $\bar{F}_{11} = \bar{F}_{22} = 1.1$  to plot these quantities against the coordinates  $\bar{F}_{12}, \bar{F}_{21} \in [-0.4, 0.4]$ . We see that the neural network function have performed a good approximation such that there is negligible difference in the macroquantities produced by surrogate model and high-fidelity solution.

Subsequently, we present in Figure 13 the stress tensor  $\bar{P}$  and tangent moduli  $\bar{C}$  for comparison between surrogate-model and FFT-based solutions. In this numerical experiment, we set  $\bar{F}_{11} = \bar{F}_{22} = 1.1, \bar{F}_{21} = -0.4$  and let  $\bar{F}_{12}$  vary in the range  $[-0.4, 0.4]$ . As expected, the isotropicity of the homogenized material is captured sufficiently well in the surrogate model and reflected via the computation of all components of  $\bar{C}$ .

In Sections 5.4 and 5.5, we examine the two-scale problems with the same microstructure of circular inclusion as the one in the present example. Thus, we can reuse the trained model in this subsection to save tremendous computation effort required for both building databases and training the neural networks. As a consequence, the algorithmic parameters characterizing the network architecture in the next two subsections are the same as those in row Example 5.3 of Table 2. A great advantage observed herein is that the existing knowledge can be exploited while improvement in accuracy of the approximate macroenergy density is still possible in future applications.

## 5.4 | Cook’s membrane problem

### 5.4.1 | Problem setting

By this numerical example, we show the robustness of the proposed surrogate model using neural networks to approximate the macroenergy density. We present comparison of the mechanical responses at the macroscale computed by the

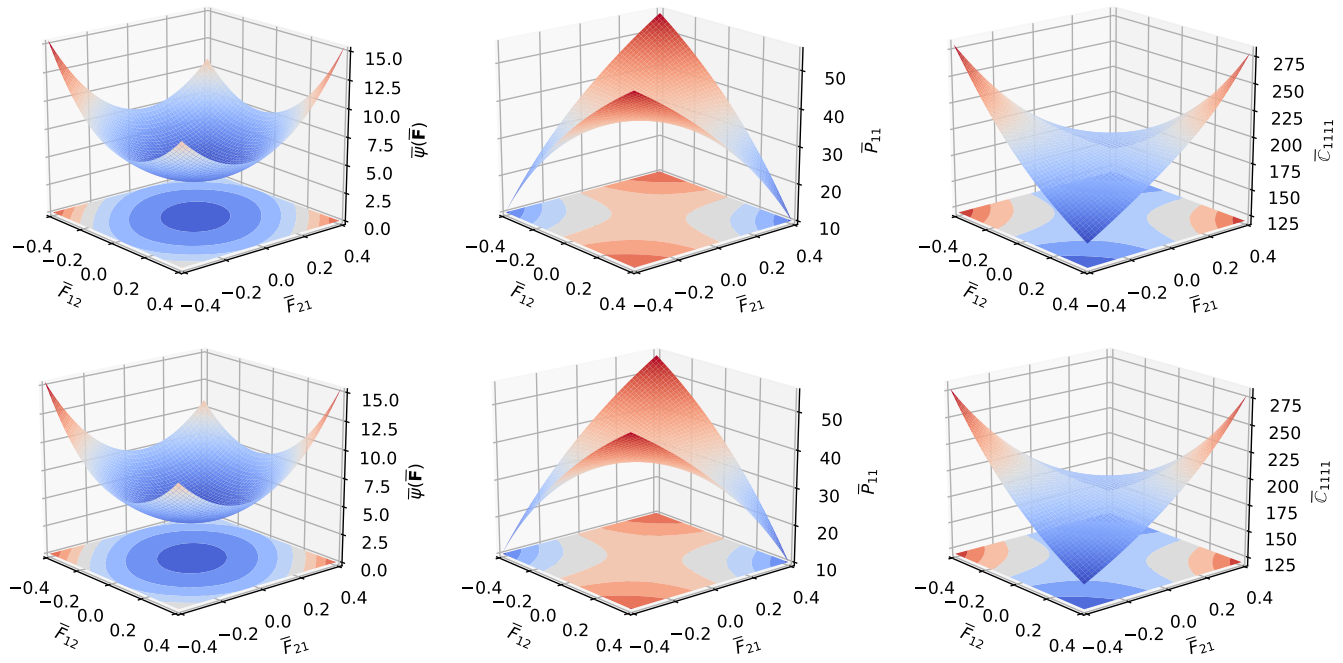


**FIGURE 11** Comparison between surrogate-model computation and high-fidelity solution. The macroenergy density (left column), the stress component  $\bar{P}_{11}$  (middle column) and the tangent moduli component  $\bar{C}_{1111}$  (right column) are ordered according to the following navigation: (top row) surrogate-model solution, (bottom row) high-fidelity solution [Colour figure can be viewed at [wileyonlinelibrary.com](http://wileyonlinelibrary.com)]

surrogate model and concurrent computations. Concretely, we investigate the well-known Cook's membrane problem whose microstructure is represented by the circular inclusion in Subsection 5.2. This problem is named after the author Cook<sup>54</sup> who first reported it. The geometry of the membrane consists of a trapezoid surface in the  $X_1$ - $X_2$  plane (see Figure 14). The structure is clamped along the left edge and it is loaded by a traction load  $\bar{q}_0 = 4$  along the right edge in the  $X_2$ -direction. The membrane is rather thick such that the plane strain assumption is valid (see also section 2.1.5, *Abaqus Benchmarks Guide*). Note that we do not aim at reproducing the Benchmark results in the aforementioned literature.

## 5.4.2 | Numerical results

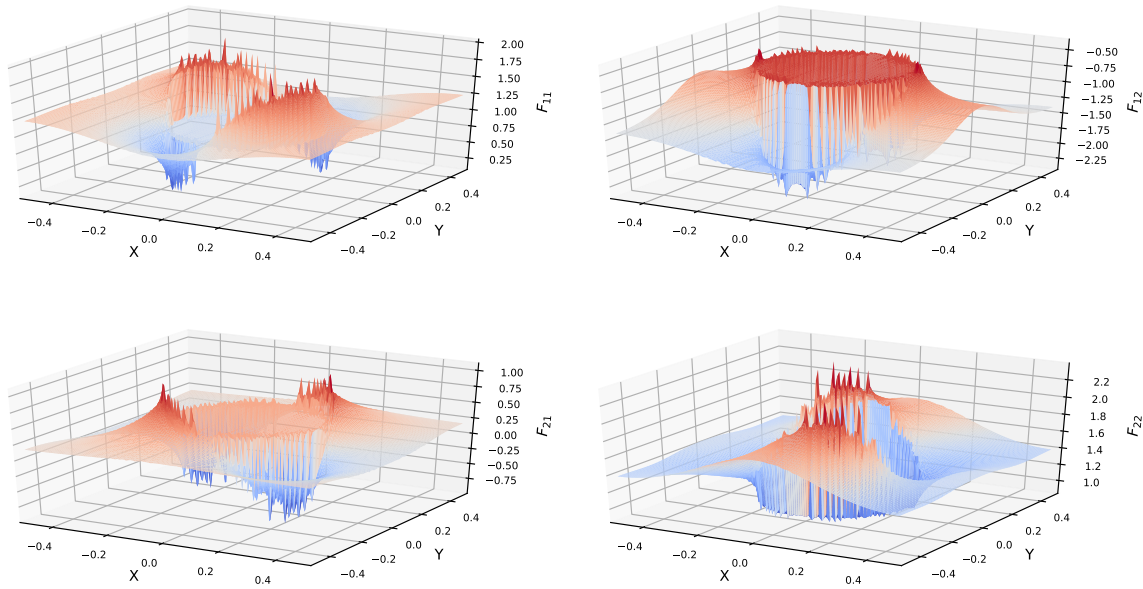
To show that the surrogate model is capable of generating numerical response that is comparable to the concurrent FE-FFT approach, we place the results of two approaches adjacent to each other. In Figures 15 and 16, the displacement fields and the resultant stresses corresponding to the surrogate model and concurrent computations are placed on the *left* and the *right*, respectively.

This example shows advantages of our surrogate model as the material data are available from the analysis of the previous example. At the macroscale the computation performs as usual, whereas at the microscale the neural network will predict the effective stresses and tangent moduli in response to the macroscopic deformation gradients evaluated at the quadrature points. So, we can avoid nested loops for solving the microscopic BVPs by FFT-based solver and the macroscopic BVP by the finite element method.

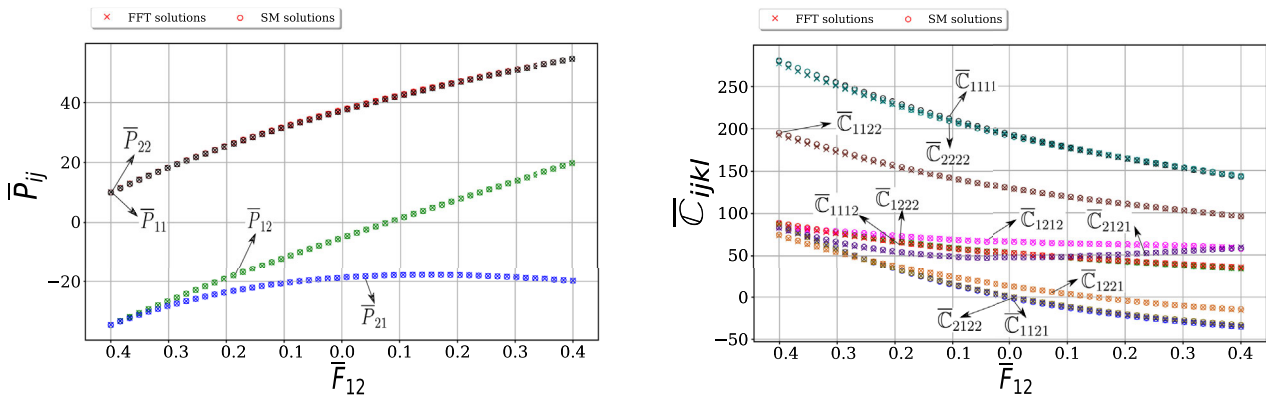
## 5.5 | Two-dimensional cantilever beam under plane strain analysis

### 5.5.1 | Problem setting

As the last example, we reaffirm the efficiency of this computational framework by providing the quantitative comparison between the full-field solution and the homogenized solution achieved by the surrogate modeling. To this end, we

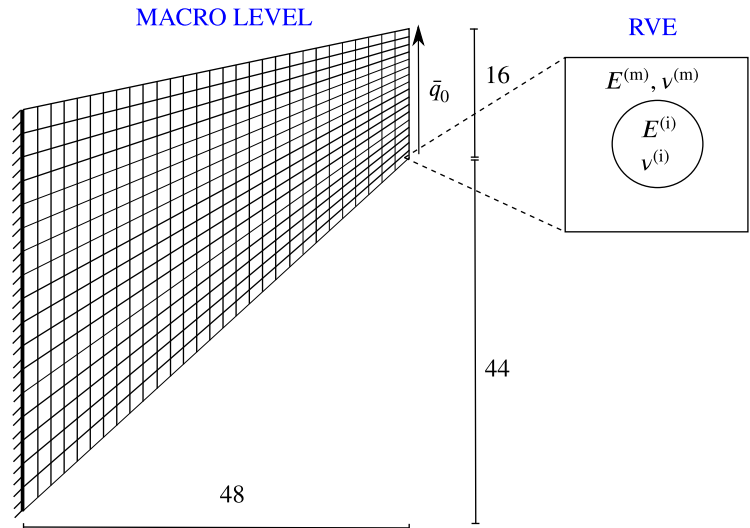


**FIGURE 12** Ringing artifacts surrounding the material interfaces in the numerical solution for a circular-inclusion RVE with macroscopic deformation gradient as  $\{\bar{F}_{11} = 1.1, \bar{F}_{12} = -1.2, \bar{F}_{21} = 0.2, \bar{F}_{22} = 1.4\}$  [Colour figure can be viewed at wileyonlinelibrary.com]



**FIGURE 13** Macroscopic stress  $\bar{P}$  and tangent moduli  $\bar{C}$ . The macroscopic stress (left) and tangent moduli (right) are produced by the surrogate model trained on  $30 \times 10^3$  data points. These tensors are compared with the counterparts produced by using the high-fidelity solution. All the numerical results are plotted against the varying component  $\bar{F}_{12} \in [-0.4, 0.4]$ , while other three components  $\bar{F}_{11} = \bar{F}_{22} = 1.1$  and  $\bar{F}_{21} = -0.4$  are kept fixed [Colour figure can be viewed at wileyonlinelibrary.com]

**FIGURE 14** Cook’s membrane problem. The Cook’s membrane is described by a two-dimensional trapezoid, clamped along the long left edge and subject to tangential traction  $\bar{q}_0 = 4$  along the right edge. The structure is constituted by the materials with microstructure of circular inclusion. The problem is analyzed in the plane strain condition [Colour figure can be viewed at wileyonlinelibrary.com]



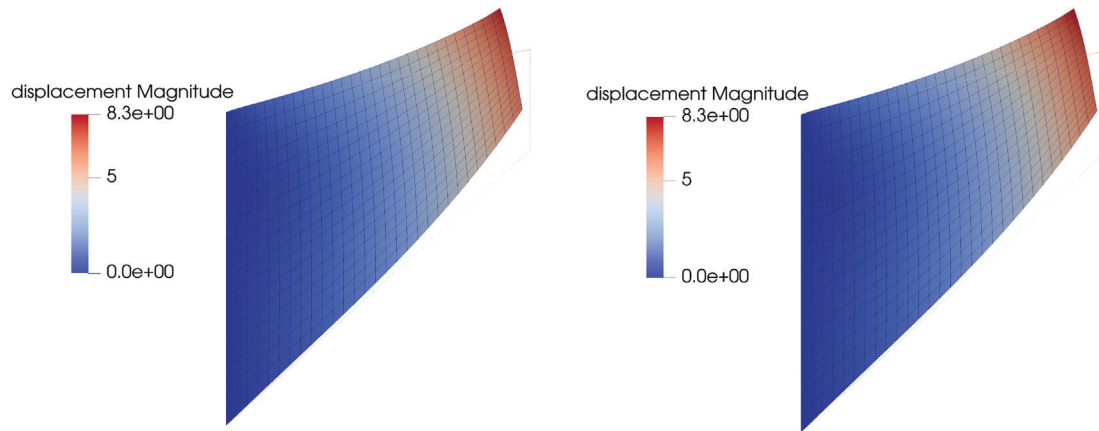


**FIGURE 15** Mechanical responses of the Cook's membrane under plane strain condition. The contour plot shows the vertical displacements computed at the macroscale according to the surrogate model (left) and to the concurrent approach (right)

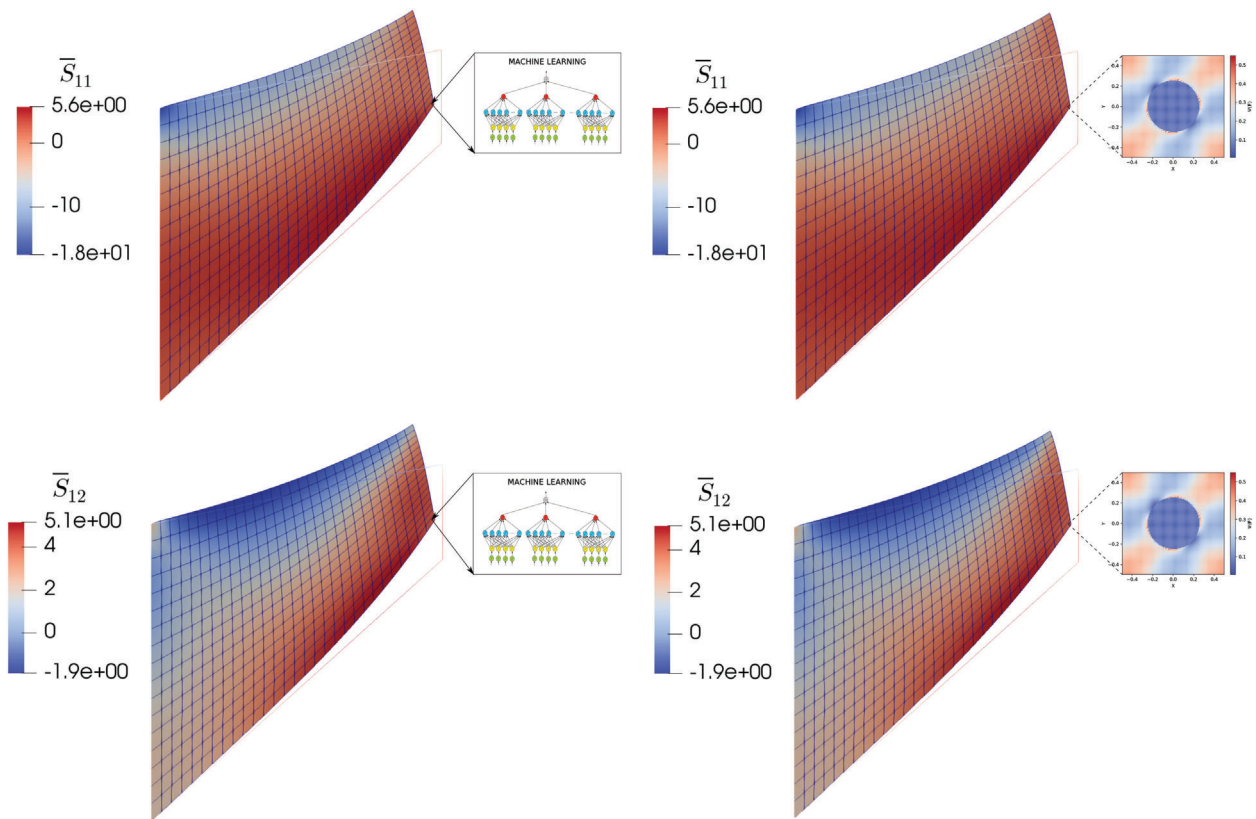


**FIGURE 16** Distribution of resultant stress within the Cook's membrane. The contour plot shows normal stress  $\bar{S}_{11}$  (top) and  $\bar{S}_{12}$  (bottom) computed at the macroscale according to the surrogate model (left) and to the two-scale approach (right), respectively

**FIGURE 17** Cantilever beam of heterogeneous materials under plane strain analysis. (Top) The beam is filled with  $40 \times 10$  circular inclusions of materials stiffer than the matrix and is subject to a traction force  $\bar{q}_0 = -0.25$ . (Bottom) When the number of inclusions approaches infinity, the RVE of circular inclusions represents well the heterogeneity of materials according to the pattern of inclusions in the top figure

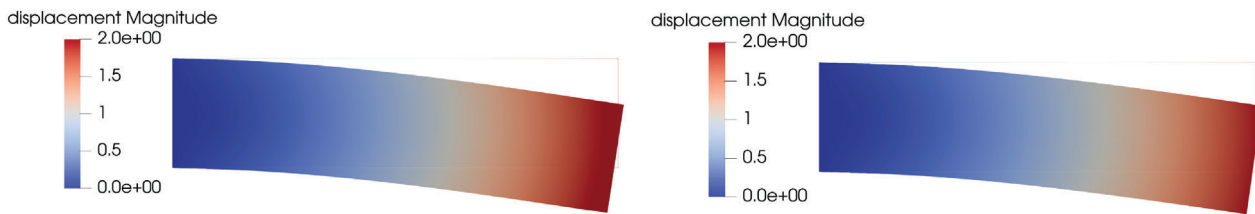
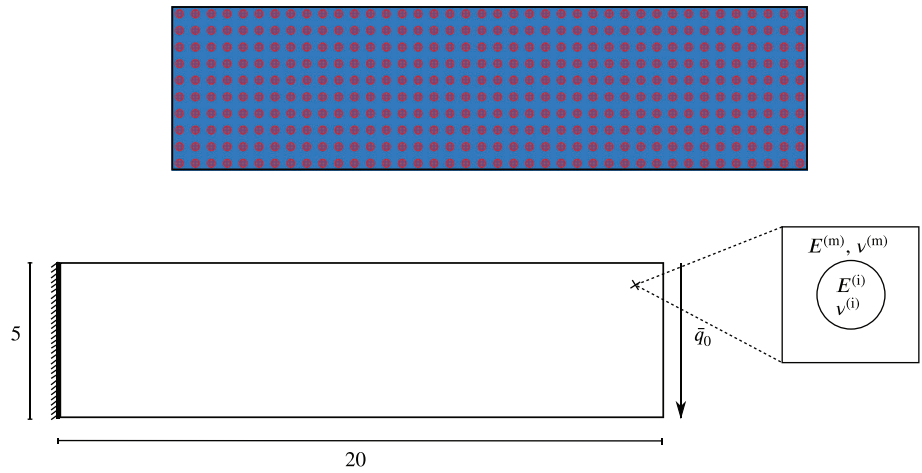


**FIGURE 18** Final deformation of the cantilever beam. The vertical displacement is contour-plotted for both the homogenized solution based on the surrogate modeling (left) and the full-field solution based on the structure with  $40 \times 10$  circular inclusions

investigate the deformation of a two-dimensional cantilever beam, once again, in plane strain analysis. The beam of rectangular geometry consists of  $N_1 \times N_2$  stiff circular inclusions, where  $N_1$  and  $N_2$  are the number of inclusions in  $X_1$ - and  $X_2$ -direction, respectively. In Figure 17 (top), one typical beam with  $(N_1 \times N_2) = (40 \times 10)$  circular inclusions is shown. For a specific mechanical setting, the beam is clamped at its left edge  $\bar{q}$  and subject to the constant tangential traction  $\bar{q}_0 = -0.25$  along its right edge, which is visualized in Figure 17 (bottom). The inclusions and matrix are made of materials given in Subsection 5.3 by Equations (50) and (51).

### 5.5.2 | Numerical results

In Figure 18, the full-field solution of the beam structure with  $40 \times 10$  circular inclusions (see Figure 17) is compared with the homogenized solution based on the surrogate model. Also in this figure, the deformed configuration of the beam as well as the contour plot of vertical displacement are shown. The agreement between the full-field solution and the homogenized solution is clearly observed.

As expected, we could notice differences in the stress distribution as the homogenized solution “averages out” the fluctuations to capture overall trend of the full-field solution. The distribution of normal second Piola stress  $\bar{S}_{11}$  obtained by surrogate modeling and full-field solution is shown in Figure 19. We observe that the overall distribution of the homogenized stress is in great compliance with the full-field stress. The ranges of stress values differ from each other as the stress field is concentrated more in the stiffer inclusion and less in the surrounding matrix. The homogenized stress basically *averages out* the fluctuations in stress values across two phases. This is reflected in Figure 19 (top) where the perturbations in values (presented by contour plot) are totally filtered out, leaving a smooth transition between neighboring points in the entire domain.

These numerical results prove the reliability of our computational framework that uses HDMM-based neural networks to construct the approximate macroenergy density.

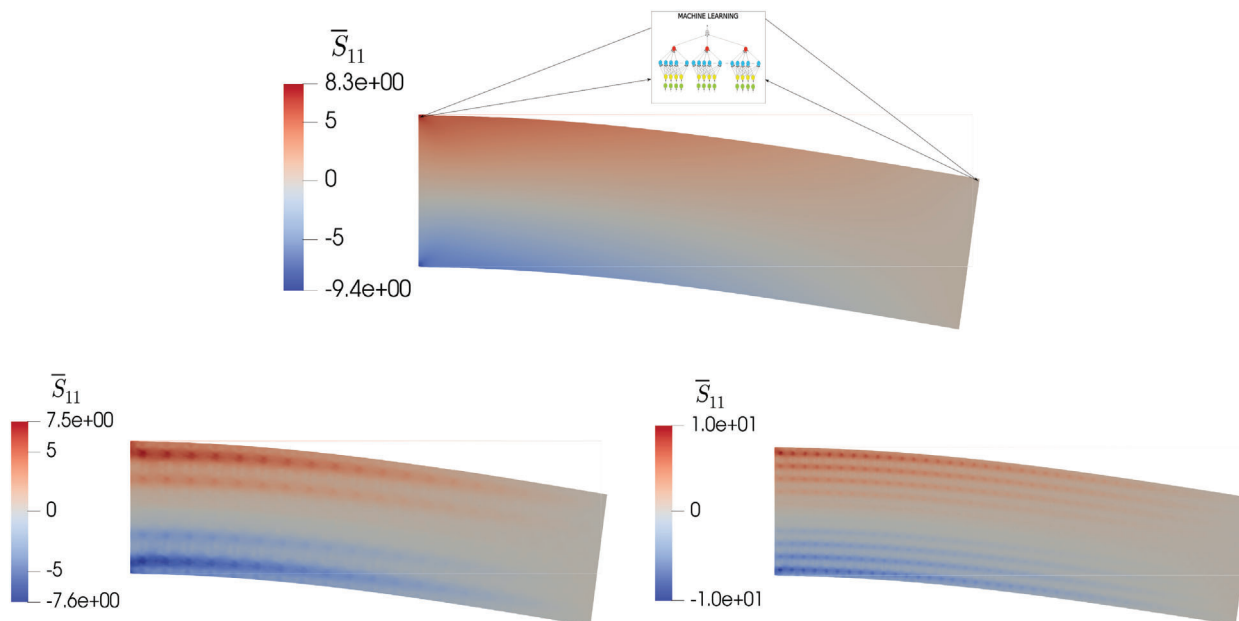


**FIGURE 19** Distribution of normal second Piola stress  $\bar{S}_{11}$ . As for cantilever beam with real circular inclusions (bottom), it is seen that the stress concentrates within the inclusions with higher intensity than that in the matrix phase. Two structures with  $20 \times 5$  and  $40 \times 10$  circular inclusions are shown in the bottom left and bottom right subfigures. As for the homogenized structure (top), the stress field appears quite smooth throughout the entire domain, just as expected

## 6 | CONCLUSION

This work proposes a surrogate model for two-scale computational homogenization. First, we pointed out that there is a strong connection between the formulation of the Lippmann-Schwinger equation for the microscopic boundary value problems by using the polarization technique and Galerkin-based projection. Indeed, the same result can be arrived at by two different derivations. We obtained new compatibility projection operators that maps an arbitrary periodic second-order tensor field to a compatible field. Second, a surrogate model for computational homogenization of elasticity at finite strains is built based on a neural network architecture that mimics high-dimensional model representation. Particularly, this black-box function is an approximator of the macroscopic energy density and is trained upon the space of uniformly distributed random data. The database is constructed by solving numerous microscopic problems with the aid of the FFT-based solver. Comparison of the numerical results with full-field solutions as well as homogenized solutions using the concurrent strategy validates the reliability and robustness of the proposed computational framework.

### ACKNOWLEDGMENTS

V.M.N.-T. thanks the sponsorship from Sofja Kovalevskaja Prize from Alexander von Humboldt Foundation (Zhuang as PI). X.Z. would like to thank the Heisenberg-Professorship from German Research Foundation (DFG). L.T.K.N. wishes to thank Felix Selim Göküzüm, Matthias Rambauser, and Marc-André Keip for introducing him to the topic computational homogenization and also for fruitful discussions during his research stay at University of Stuttgart as well as the financial support from DFG for the Cluster of Excellence in Simulation Technology (EXC 310).

### CONFLICT OF INTEREST

The authors declare that there are no known conflicts of interest associated with this publication and there has been no significant financial support for this work that could have prohibited its outcome.

### ORCID

Lu Trong Khiem Nguyen  <https://orcid.org/0000-0002-5546-457X>

Timon Rabczuk  <https://orcid.org/0000-0002-7150-296X>

Xiaoying Zhuang  <https://orcid.org/0000-0001-6562-2618>

## REFERENCES

1. Hashin Z, Shtrikman S. A variational approach to the theory of the elastic behaviour of polycrystals. *J Mech Phys Solids*. 1962;10(4):343-352. [https://doi.org/10.1016/0022-5096\(62\)90005-4](https://doi.org/10.1016/0022-5096(62)90005-4).
2. Hashin Z, Shtrikman S. A variational approach to the theory of the elastic behaviour of multiphase materials. *J Mech Phys Solids*. 1963;11(2):127-140. [https://doi.org/10.1016/0022-5096\(63\)90060-7](https://doi.org/10.1016/0022-5096(63)90060-7).
3. Willis JR. Bounds and self-consistent estimates for the overall properties of anisotropic composites. *J Mech Phys Solids*. 1977;25(3):185-202. [https://doi.org/10.1016/0022-5096\(77\)90022-9](https://doi.org/10.1016/0022-5096(77)90022-9).
4. Willis JR. Variational and related methods for the overall properties of composites. *Advances in Applied Mechanics*. Vol 21. Elsevier; 1981:1-78. [https://doi.org/10.1016/S0065-2156\(08\)70330-2](https://doi.org/10.1016/S0065-2156(08)70330-2).
5. Avellaneda M. Optimal bounds and microgeometries for elastic two-phase composites. *SIAM J Appl Math*. 1987;47(6):1216-1228. <https://doi.org/10.1137/0147082>.
6. Milton GW, Kohn RV. Variational bounds on the effective moduli of anisotropic composites. *J Mech Phys Solids*. 1988;36(6):597-629. [https://doi.org/10.1016/0022-5096\(88\)90001-4](https://doi.org/10.1016/0022-5096(88)90001-4).
7. Castañeda PP. The effective mechanical properties of nonlinear isotropic composites. *J Mech Phys Solids*. 1991;39(1):45-71. [https://doi.org/10.1016/0022-5096\(91\)90030-R](https://doi.org/10.1016/0022-5096(91)90030-R).
8. Willis JR. The overall elastic response of composite materials. *J Appl Mech*. 1983;50(4b):1202-1209. <https://doi.org/10.1115/1.3167202>.
9. Talbot DRS, Willis JR. Variational principles for inhomogeneous non-linear media. *IMA J Appl Math*. 1985;35(1):39-54. <https://doi.org/10.1093/imamat/35.1.39>.
10. Ponte CP, Willis JR. On the overall properties of nonlinearly viscous composites. *Proc Royal Soc Lond A Math Phys Sci*. 1988;416(1850):217-244. <https://doi.org/10.1098/rspa.1988.0035>.
11. Castañeda PP, Suquet P. Nonlinear composites. *Advances in Applied Mechanics*. Vol 34. Elsevier; 1997:171-302. [https://doi.org/10.1016/S0065-2156\(08\)70321-1](https://doi.org/10.1016/S0065-2156(08)70321-1).
12. Milton GW. *The Theory of Composites*. Cambridge Monographs on Applied and Computational Mathematics. Cambridge University Press; 2002. <https://doi.org/10.1017/CBO9780511613357>.
13. Hughes TJR, Feijóo GR, Mazzei L, Quincy J-B. The variational multiscale method-a paradigm for computational mechanics. *Comput Methods Appl Mech Eng*. 1998;166(1):3-24. [https://doi.org/10.1016/S0045-7825\(98\)00079-6](https://doi.org/10.1016/S0045-7825(98)00079-6).
14. Miehe C, Schröder J, Schotte J. Computational homogenization analysis in finite plasticity Simulation of texture development in polycrystalline materials. *Comput Methods Appl Mech Eng*. 1999;171(3):387-418. [https://doi.org/10.1016/S0045-7825\(98\)00218-7](https://doi.org/10.1016/S0045-7825(98)00218-7).
15. Feyel F. Multiscale FE2 elastoviscoplastic analysis of composite structures. *Comput Mater Sci*. 1999;16(1):344-354. [https://doi.org/10.1016/S0927-0256\(99\)00077-4](https://doi.org/10.1016/S0927-0256(99)00077-4).
16. Mandel J. Plasticité classique et viscoplasticité: course held at the department of mechanics of solids, September-October, 1971. courses and lectures - International Centre for Mechanical Sciences, Springer-Verlag; New York, NY: 1972.
17. Hill R. On constitutive macro-variables for heterogeneous solids at finite strain. *Proceedings of the Royal Society of London A. Mathematical and Physical Sciences*. 1972;326(1565):131-147. <https://doi.org/10.1098/rspa.1972.0001>.
18. Geers MGD, Kouznetsova VG, Brekelmans WAM. Multi-scale computational homogenization: trends and challenges. *J Comput Appl Math*. 2010; 234, 234;(7):2175-2182. <https://doi.org/10.1016/j.cam.2009.08.077>.
19. Allaire G. Homogenization and two-scale convergence. *SIAM J Math Anal*. 1992;23(6):1482-1518. <https://doi.org/10.1137/0523084>.
20. Fish J, Shek K, Pandheeradi M, Shephard MS. Computational plasticity for composite structures based on mathematical homogenization: theory and practice. *Comput Methods Appl Mech Eng*. 1997;148(1):53-73. [https://doi.org/10.1016/S0045-7825\(97\)00030-3](https://doi.org/10.1016/S0045-7825(97)00030-3).
21. Fish J, Yang Z, Yuan Z. A second-order reduced asymptotic homogenization approach for nonlinear periodic heterogeneous materials. *Int J Numer Methods Eng*. 2019;119(6):469-489. <https://doi.org/10.1002/nme.6058>.
22. Moulinec H, Suquet P. A numerical method for computing the overall response of nonlinear composites with complex microstructure. *Comput Methods Appl Mech Eng*. 1998;157(1):69-94. [https://doi.org/10.1016/S0045-7825\(97\)00218-1](https://doi.org/10.1016/S0045-7825(97)00218-1).
23. Moulinec H, Suquet P. A fast numerical method for computing the linear and nonlinear mechanical properties of composites. *Comptes rendus de l'Académie des sciences. Série II, Mécanique, physique, chimie, astronomie*. 1994;318(11):1417-1423.
24. Vidyasagar A, Tan WL, Kochmann DM. Predicting the effective response of bulk polycrystalline ferroelectric ceramics via improved spectral phase field methods. *J Mech Phys Solids*. 2017; 106(106):133-151. <https://doi.org/10.1016/j.jmps.2017.05.017>.
25. Cooley JW, Tukey JW. An algorithm for the machine calculation of complex Fourier series. *Math Comput*. 1965;19(90):297-301.
26. Zeman J, Vondřejc J, Novák J, Marek I. Accelerating a FFT-based solver for numerical homogenization of periodic media by conjugate gradients. *J Comput Phys*. 2010;229(21):8065-8071. <https://doi.org/10.1016/j.jcp.2010.07.010>.
27. Michel JC, Moulinec H, Suquet P. A computational scheme for linear and non-linear composites with arbitrary phase contrast. *Int J Numer Methods Eng*. 2001;52(1-2):139-160. <https://doi.org/10.1002/nme.275>.
28. Brisard S, Dormieux L. Combining Galerkin approximation techniques with the principle of Hashin and Shtrikman to derive a new FFT-based numerical method for the homogenization of composites. *Comput Methods Appl Mech Eng*. 2012;217: 197-220. <https://doi.org/10.1016/j.cma.2012.01.003>.
29. Geus TWJ, Vondřejc J, Zeman J, Peerlings RHJ, Geers MGD. Finite strain FFT-based non-linear solvers made simple. *Comput Methods Appl Mech Eng*. 2017;318:412-430. <https://doi.org/10.1016/j.cma.2016.12.032>.
30. Göküzüm FS, Nguyen LTK, Keip M-A. A multiscale FE-FFT framework for electro-active materials at finite strains. *Comput Mech*. 2019; 64:63-84. <https://doi.org/10.1007/s00466-018-1657-7>.

31. Rambašek M, Göküzüm FS, Nguyen LTK, KM-A. A two-scale FE-FFT approach to nonlinear magneto-elasticity. *Int J Numer Methods Eng*. 2019;117(11):1117-1142. <https://doi.org/10.1002/nme.5993>.
32. Göküzüm FS, Keip M-A. An algorithmically consistent macroscopic tangent operator for FFT-based computational homogenization. *Int J Numer Methods Eng*. 2018;113(4):581-600. <https://doi.org/10.1002/nme.5627>.
33. Zeman J, Geus TWJ, Vondřejc J, Peerlings RHJ, Geers MGD. A finite element perspective on nonlinear FFT-based micromechanical simulations. *Int J Numer Methods Eng*. 2017;111(10):903-926. <https://doi.org/10.1002/nme.5481>.
34. Yvonnet J, He Q-C. The reduced model multiscale method (R3M) for the non-linear homogenization of hyperelastic media at finite strains. *J Comput Phys*. 2007;223(1):341-368. <https://doi.org/10.1016/j.jcp.2006.09.019>.
35. Fritzen F, Kunc O. Two-stage data-driven homogenization for nonlinear solids using a reduced order model. *Europ J Mech A/Solids*. 2018;69:201-220. <https://doi.org/10.1016/j.euromechsol.2017.11.007>.
36. Oskay C, Fish J. Eigendeformation-based reduced order homogenization for failure analysis of heterogeneous materials. *Comput Methods Appl Mech Eng*. 2007;196(7):1216-1243.
37. Le BA, Yvonnet J, He Q-C. Computational homogenization of nonlinear elastic materials using neural networks. *Int J Numer Methods Eng*. 2015;104(12):1061-1084. <https://doi.org/10.1002/nme.4953>.
38. Manzhos S, Carrington T. A random-sampling high dimensional model representation neural network for building potential energy surfaces. *J Chem Phys*. 2006;125(8):084109. <https://doi.org/10.1063/1.2336223>.
39. Borst R, Crisfield MA, Remmers JJC, Verhoosel CV. *Non-Linear Finite Element Analysis of Solids and Structures*. John Wiley & Sons, Ltd; 2012. <https://onlinelibrary.wiley.com/doi/book/10.1002/9781118375938>.
40. Miehe C, Vallicotti D, Teichtmeister S. Homogenization and multiscale stability analysis in finite magneto-electro-elasticity. application to soft matter EE, ME and MEE composites. *Comput Methods Appl Mech Eng*. 2016;300:294-346. <https://doi.org/10.1016/j.cma.2015.10.013>.
41. Trefethen LN. *Approximation Theory and Approximation Practice*. Philadelphia, Pennsylvania Society for Industrial and Applied Mathematics; 2012. <https://dl.acm.org/doi/book/10.5555/2430658>.
42. Terada K, Hori M, Kyoya T, Kikuchi N. Simulation of the multi-scale convergence in computational homogenization approaches. *Int J Solids Struct*. 2000;37(16):2285-2311. [https://doi.org/10.1016/S0020-7683\(98\)00341-2](https://doi.org/10.1016/S0020-7683(98)00341-2).
43. Fish J, Kuznetsov S. Computational continua. *Int J Numer Methods Eng*. 2010;84(7):774-802. <https://doi.org/10.1002/nme.2918>.
44. Stein EM, Shakarchi R. *Fourier Analysis: An Introduction*. Princeton, NJ: Princeton University Press; 2011.
45. Manzhos S, Yamashita K, Carrington T. Fitting sparse multidimensional data with low-dimensional terms. *Comput Phys Commun*. 2009;180(10):2002-2012. <https://doi.org/10.1016/j.cpc.2009.05.022>.
46. Stein EM, Shakarchi R. *Real Analysis Measure Theory, Integration, and Hilbert Spaces*. Princeton, NJ: Princeton University Press; 2005.
47. Goodfellow Ian J., Bengio Yoshua, Courville Aaron. *Deep Learning*. Cambridge, MA: MIT Press; 2016. <http://www.deeplearningbook.org>.
48. Wang K, Sun WC. A multiscale multi-permeability poroplasticity model linked by recursive homogenizations and deep learning. *Comput Methods Appl Mech Eng*. 2018;334:337-380. <https://doi.org/10.1016/j.cma.2018.01.036>.
49. Srivastava N, Hinton G, Krizhevsky A, Sutskever I, Salakhutdinov R. Dropout: a simple way to prevent neural networks from overfitting. *J Mach Learn Res*. 2014;15(1):1929-1958.
50. Nguyen L, Trong K, Rambašek M, Keip M-A. Variational framework for distance-minimizing method in data-driven computational mechanics. *Comput Methods Appl Mech Eng*. 2020;365:112898. <https://doi.org/10.1016/j.cma.2020.112898>.
51. Yvonnet J, Monteiro E, He Q-C. Computational homogenization method and reduced database model for hyperelastic heterogeneous structures. *Int J Multiscale Comput Eng*. 2013;11(3):201-225. <https://doi.org/10.1615/IntJMultCompEng.2013005374>.
52. Rovinelli A, Proudhon H, Lebensohn RA, Sangid MD. Assessing the reliability of fast Fourier transform-based crystal plasticity simulations of a polycrystalline material near a crack tip. *Int J Solids Struct*. 2020;184:153-166. <https://doi.org/10.1016/j.ijsolstr.2019.02.024>.
53. Ma R, Sun WC. FFT-based solver for higher-order and multi-phase-field fracture models applied to strongly anisotropic brittle materials. *Comput Methods Appl Mech Eng*. 2020;362:112781. <https://doi.org/10.1016/j.cma.2019.112781>.
54. Cook RD. Improved two-dimensional finite element. *J Struct Div*. 1974;100(9):1851-1863.

## SUPPORTING INFORMATION

Additional supporting information may be found online in the Supporting Information section at the end of this article.

**How to cite this article:** Nguyen-Thanh VM, Trong Khiem Nguyen L, Rabczuk T, Zhuang X. A surrogate model for computational homogenization of elastostatics at finite strain using high-dimensional model representation-based neural network. *Int J Numer Methods Eng*. 2020;121:4811-4842. <https://doi.org/10.1002/nme.6493>